High-spin states, particle-hole structure, and linked smooth terminating bands in doubly odd ^{112}Sb

G. J. Lane,* D. B. Fossan, C. J. Chiara, H. Schnare,† J. M. Sears, J. F. Smith,‡ I. Thorslund, and P. Vaska§
Department of Physics and Astronomy, State University of New York at Stony Brook, New York 11794-3800

E. S. Paul, A. N. Wilson,‖ and J. N. Wilson¶
Oliver Lodge Laboratory, University of Liverpool, Liverpool L69 7ZE, United Kingdom

K. Hauschild,** I. M. Hibbert,†† and R. Wadsworth
Department of Physics, University of York, Heslington Y01 5DD, United Kingdom

A. V. Afanasjev‡‡ and I. Ragnarsson
Department of Mathematical Physics, Lund Institute of Technology, Box 118, S-22100 Lund, Sweden
(Received 4 February 1998)

Excited states in ^{112}Sb have been observed with the Stony Brook array of six Compton-suppressed HPGe detectors and the ^{103}Rh(^{12}C,3n) reaction at 60 MeV using a thick target. New excited states which decay solely towards the $\tau_m = 773$ ns, $I^\pi = 8^-$ isomer have been identified using time-correlated spectroscopy. The previously known level scheme has also been extended and corrected. In total, five rotational bands are observed, consisting of the two previously known strongly coupled bands based upon one-particle–one-hole (1p-1h) proton excitations across the $Z = 50$ shell gap and three newly observed decoupled bands based upon 2p-2h proton excitations. The 1p-1h bands are interpreted as deformed rotors, although there is a possibility that a shears mechanism like that observed in the lead region may also play a role. Results from a thin-target measurement using the Eurogam-II spectrometer and the ^{90}Zr(^{31}P,2αn) reaction at 150 MeV are also presented. These data have been used to extend the decoupled bands up to $I \sim 40\hbar$, a spin regime where the bands exhibit the features of smooth band termination. The combined results from the two experiments have enabled two of the bands to be connected by discrete γ-ray transitions to the low-spin level scheme, thereby determining their spins and parities. This allows for a definitive comparison with the results of cranked Nilsson-Strutinsky calculations and excellent agreement is obtained. Further confirmation of the terminating band configuration assignments is obtained from an analysis of the relative alignment properties of pairs of bands in the chain $^{110-112}$Sb. [S0556-2813(98)02007-X]

PACS number(s): 21.10.Re, 21.10.Tg, 23.20.Lv, 27.60.+j

I. INTRODUCTION

Studies of the nuclei with $Z \approx 50$ have yielded important and interesting physics in terms of low-lying collective structures which coexist with the expected single-particle states [1,2]. Such collectivity was observed initially in the odd-mass antimony [3] and even-mass tin [4] nuclei, where prolate shapes are stabilized by proton particle-hole (p-h) excitations across the $Z = 50$ shell gap, from the β-upsloping $g_{9/2}$ orbital into the β-downsloping $g_{7/2}/d_{5/2}$ and $h_{11/2}$ orbitals. Many cases of deformed rotational bands in this region are now known, although it is only more recently that the added power of the new large γ-ray detector arrays has been brought to bear on these collective structures. Such studies [5–11] have enabled the investigation of the demise of the collectivity of the deformed rotational bands which occurs due to the limited angular momentum available to the underlying single-particle configurations [12]. The limited valence space available to the collective structures is due to the proximity of the doubly closed shell, so that, with one to three proton holes in the $g_{9/2}$ shell, the total angular momentum of the valence nucleons for nuclei in the $A \approx 110$ region is limited to $\sim(30-50)\hbar$. As the spin increases within a collective band, the valence nucleons align with the rotational axis, resulting in a gradual change of the nuclear shape with increasing spin from collective near prolate ($\gamma \approx 0°$) at low spin to noncollective oblate ($\gamma = +60°$) when all the nucleons within the configuration are fully aligned [13,14]. Thus, collective bands built upon core-excited configurations terminate eventually at a spin corresponding to the sum of the

*Present address: Department of Nuclear Physics, R.S. Phys. S.E., Australian National University, Canberra ACT 0200, Australia.
†Present address: Institut für Kern- und Hadronenphysik, Forschungszentrum Rossendorf, D-01314 Dresden, Germany.
‡Present address: Department of Physics, University of Manchester, Manchester M13 9PL, United Kingdom.
§Present address: UGM Laboratory, Inc., 3611 Market St., Philadelphia, PA 19107.
‖Present address: Department of Physics, University of York, Heslington Y01 5DD, United Kingdom.
¶Present address: Chemistry Department, Washington University, St. Louis, MO 63130.
**Present address: Lawrence Livermore Laboratory, P.O. Box 808, Livermore, CA 94550.
††Present address: Oliver Lodge Laboratory, University of Liverpool, Liverpool L69 7ZE, United Kingdom.
‡‡Permanent address: Nuclear Research Center, Latvian Academy of Sciences, LV-2169, Salaspils, Mierastr. 31, Latvia.

spins of the individual valence nucleons. The best examples of this *smooth band termination* phenomenon occur for nuclei with the right balance of a sufficient number (10–15) of nucleons outside of ^{100}Sn to develop collectivity, yet close enough to ^{100}Sn to ensure that the termination of the bands can occur both near yrast and at an experimentally attainable spin value. Excellent examples are found in ^{109}Sb [6] and other nuclei in its immediate vicinity, including ^{108}Sn [7] and ^{110}Sb [10].

The observed smooth terminating bands show an increase of the γ-ray energy spacing with increasing spin. This corresponds to a falloff in the dynamic moment of inertia $\mathcal{J}^{(2)}$ with increasing rotational frequency such that unusually low values of $\mathcal{J}^{(2)}$ ($\frac{1}{3}-\frac{1}{2}$ of the rigid-body value) are observed at high spin. In addition, it leads to characteristic minima in plots of the state energies with a rigid-rotor reference subtracted ($E-E_{\mathrm{RLD}}$) [5–11]. Experimental evidence for the gradual shape change and associated loss in collectivity with increasing spin has been obtained only recently in the form of transition quadrupole moments for smooth terminating bands in ^{108}Sn [15], ^{109}Sb [15], and, in a different mass region, ^{62}Zn [16]. The theoretical description of smooth band termination [13,14] has relied primarily upon the cranked Nilsson-Strutinsky model and there is substantial evidence that this model provides a good understanding of the main experimental features; nevertheless, it is important to test the limits of applicability of the theory. As the nuclear Fermi level changes, smooth terminating bands with various single-particle configurations and different theoretically predictable characteristics approach the yrast line. A good theoretical description of these changing features will give confidence that the understanding is correct. It was demonstrated recently that theoretical calculations have predictive powers, when a smooth terminating band in ^{110}Sb [10] was shown to be in excellent agreement with prior calculations [14]. An important feature of that work was that the yrast band was connected by discrete γ-ray transitions to the low-spin-level scheme, giving well-determined spins and allowing for a definitive comparison with theory; in many cases spin and parity measurements have not been possible (e.g., Refs. [5,6]). A further constraint and test of the theory are obtained by linking multiple smooth terminating bands into the low-spin-level scheme. As yet, there are only two cases (^{108}Sn [7] and ^{109}Sn [8]) for which such comparisons can be made. The new results presented here for two linked decoupled bands in ^{112}Sb, and another band which is a likely signature partner of a linked band, provides a unique test of the theory. The data are compared with the results of cranked Nilsson-Strutinsky calculations and excellent agreement is obtained.

Another area of recent interest is the phenomenon of shears bands. Observed originally in the lead region (see Refs. [17–19] and references therein), the antimony isotopes are predicted [20] to be good examples of this structural feature due to the proximity to the Fermi surface of high-K, $g_{9/2}$ proton holes and low-K, $h_{11/2}$ neutron particles. Two bands with these active orbitals (configurations involving 1p-1h proton excitations) have been identified in ^{112}Sb in the current work. The present article uses the geometric model to reproduce the experimental properties of the bands, without the need to invoke the shears mechanism. Further tilted-axis cranking calculations [21] are currently in progress for the odd-odd antimony isotopes to determine the conditions under which shears bands can occur [22].

Excited states in ^{112}Sb have been investigated on a number of previous occasions using various experimental methods. Low-spin states have been studied using light-ion reactions [(p,n) and $(^3\mathrm{He},xn)$ [23,24]] and radioactive-decay techniques [25]. Two high-spin studies have also been reported recently [26,27]. The current work expands considerably upon these previous investigations.

II. EXPERIMENTAL DETAILS

Excited states in ^{112}Sb were populated in two complementary experiments. The first experiment used a six-detector array and was designed to populate ^{112}Sb preferentially, especially the yrast and near-yrast states up to moderate spin. A light-ion reaction and a thick target were used to achieve this goal. The second experiment used a large detector array and employed a heavy beam and thin target, populating high-spin states in ^{112}Sb via a weakly populated $2\alpha n$ evaporation channel. Further details regarding both experiments are presented below.

A. Thick-target experiment

High-spin states in ^{112}Sb were populated using the ^{103}Rh(^{12}C,3n) reaction at 60 MeV, with the ^{12}C ions provided by the Stony Brook FN tandem/superconducting LINAC. An excitation function determined that a beam energy of 60 MeV was appropriate, with the $3n$ and $p2n$ channels leading to ^{112}Sb and ^{112}Sn, respectively, populated with the strongest (approximately equal) intensity. A thick target of natural rhodium was used, and the consequent integration of the fusion cross section down to the Coulomb barrier ($V_C \approx 40$ MeV), together with the light-ion nature of the ^{12}C beam, meant that substantial side feeding was obtained down to the lowest-spin states. Although the compound nuclei were only formed with maximum spins of $(20-25)\hbar$, the side feeding and resultant population of both yrast and near-yrast states meant that a comprehensive level scheme could be constructed. This was helpful for the identification of the linking transitions between two of the decoupled bands and the rest of the level scheme, as will be discussed in Sec. IV.

The γ rays emitted in the reaction were detected using the Stony Brook array of six Compton-suppressed HPGe detectors, each 25–30 % efficient, arranged in a horizonal plane. A 14-element array of hexagonal bismuth germanate (BGO) detectors subtending 80% of 4π was also used as a γ-ray multiplicity filter. The LINAC was run in a swept mode whereby two out of every three beam pulses were suppressed with a high-voltage beam sweeper. The resulting time structure for the beam consisted of <1 ns wide pulses separated by 318 ns so as to accomodate delayed coincidence measurements. This also enabled a ± 159 ns γ-ray coincidence overlap to be employed, long enough to include the low-energy γ rays and x rays which experience a time walk in the Ge detectors. The data written to magnetic tape included the coincident γ-ray energies from the Ge detectors (minimum fold $=2$), the total γ-ray energy and multiplicity measured in the BGO filter, and the times of detection of each γ ray

relative to the beam pulse. Approximately 140×10^6 coincidence events were collected.

B. Thin-target experiment

High-spin states in ^{112}Sb were also populated using the ^{90}Zr(^{31}P,$2\alpha n$) reaction at 150 MeV, with the beam of ^{31}P ions provided by the Vivitron electrostatic accelerator at Strasbourg. The experiment was originally designed to investigate high-spin states in the strongly populated $2p2n$ and $\alpha p2n$ channels leading to ^{117}I [28] and ^{114}Te [11], respectively. The $2\alpha n$ channel leading to ^{112}Sb was more weakly populated, comprising $\sim3\%$ of the total fusion cross section.

The γ rays emitted in the reaction were detected with the Eurogam-II spectrometer, consisting of 54 large volume Compton-suppressed HPGe detectors. Of this total, 30 were large-volume (75% efficient) single-crystal detectors situated at forward/backward angles with respect to the beam axis, while 24 were ''clover'' [29] detectors (four elements, each 21% efficient) situated near 90°. Two stacked self-supporting targets of ^{90}Zr ($>97\%$ enriched) were used, each with nominal thickness of 440 μg/cm^2. With a trigger condition of $n\geqslant5$ unsuppressed γ rays in coincidence, approximately 850×10^6 high-fold γ^n coincidence events were recorded on magnetic tape. Despite the weak cross section for the population of ^{112}Sb, the quality of the high-fold data and the use of a thin target meant that it was possible to apply multiple gates on the high-fold coincidence data and observe the collective bands in ^{112}Sb to high spin.

III. ANALYSIS METHODS

A. Thick-target experiment

During replay, the data were sorted in a variety of ways to create γ-ray spectra and γ-ray coincidence matrices, which were subsequently analyzed using the RADWARE software package [30]. The following sorting methods were applied.

(i) γ-γ coincidence matrices were sorted with suitable gates placed on the γ-ray multiplicity (K) and total energy (H) measured in the BGO filter. This was to enhance the fusion evaporation reactions (which have a high multiplicity) and suppress the γ-ray coincidence events due to Coulomb excitation and radioactive decay (which generally have a low multiplicity). Typically the condition $K\geqslant1$ was used. The symmetrized matrices, including those discussed below, were analyzed using the ESCL8R code [30] to project background-subtracted, gated coincidence spectra.

(ii) γ-γ coincidence matrices were sorted with various conditions placed on the γ-ray times. Gates were set on the time spectrum for each detector corresponding to ±15 ns around the beam pulse (prompt) and >15 ns after the beam pulse (delayed). Symmetrized matrices consisting of prompt-prompt and delayed-delayed coincidences were created. An unsymmetrized prompt-delayed matrix was also created, thus enabling the temporal ordering of pairs of γ rays coincident across an isomer. H and K cuts were not used for the delayed-delayed and prompt-delayed matrices, since that could suppress low-multiplicity events caused by the decay of long-lived isomeric states.

(iii) The γ-γ coincidence data were projected into three different spectra according to the angles of the detectors. The Stony Brook array has six detectors in a planar arrangement, and so the data were sorted into the angular groupings $(26°,-25°)$, $(80°,-91°)$, and $(144°,-142°)$. H and K cuts were placed as in (i) above to suppress low-multiplicity events. The intensities of the γ rays in these angular spectra were determined and then fitted with the standard expression $W(\theta)=1+A_2P_2(\cos\theta)$. Note that the overall intensity normalization has been omitted and that with three effective detector angles only the A_2 coefficient could be determined. Strictly speaking, these are not true angular distributions because the intensities are taken from the coincidence data. Nevertheless, the signs of the anisotropies can still be used to help deduce the multipolarities of transitions.

(iv) The γ-γ coincidence data were also sorted into an angular correlation matrix, where the data from the 80° and $-91°$ detectors ($\sim90°$) were placed on one axis, with the coincident γ rays detected at the forward/backward (FB) angles sorted onto the opposite axis. H and K cuts were placed on the data as described in (i) above. The experimental ratio given by

$$R_{\rm DCO}=\frac{I_\gamma(\text{observed at FB angles, gate on }\sim90°)}{I_\gamma(\text{observed at }\sim90°\text{, gate on FB angles})} \quad (1)$$

was measured and the method of directional correlations from oriented states (DCO) [31] was used to interpret these data.

B. Thin-target experiment

With the use of a thin target, γ rays emitted from the nuclei recoiling out of the target experience the full Doppler shift. During sorting of the Eurogam-II thin-target data, the γ-ray energies were Doppler corrected before being sorted in a variety of ways, including the following.

(i) The data were unfolded off line into approximately 13×10^9 triple coincidences which were incremented into a three-dimensional histogram (cube). The LEVIT8R code [30] was then used to project double-gated, background-subtracted coincidence spectra from the cube and determine the coincidence relationships between γ rays.

(ii) The data were also sorted into a gated DCO matrix. A gate list consisting of transitions with energies 932, 1003, 1059, 1117, 1183, 1299, 1494, 1696, 1871, and 2047 keV was chosen so as to enhance the intensity of the most strongly populated decoupled band in ^{112}Sb. The gating procedure involved unfolding the data into dual coincidences, each of which was only incremented into the matrix if at least one of the rest of the γ rays in the coincidence event satisfied one of the gating conditions. The γ rays detected in the ten coaxial detectors at 22.4° and 157.7° were sorted onto one axis, while γ rays detected in the 24 clover detectors at 104.5° and 75.5° were sorted onto the other axis. The effect of the matrix gating procedure on the angular correlation ratios is minimal, since the gating transitions were allowed to be observed at any angle so that the extraneous correlation effects average to zero.

(iii) The linear polarizations of γ rays were extracted for some of the transitions associated with the strongest decoupled band in ^{112}Sb by using the clover detectors as Compton polarimeters [29]. Two matrices were constructed from the

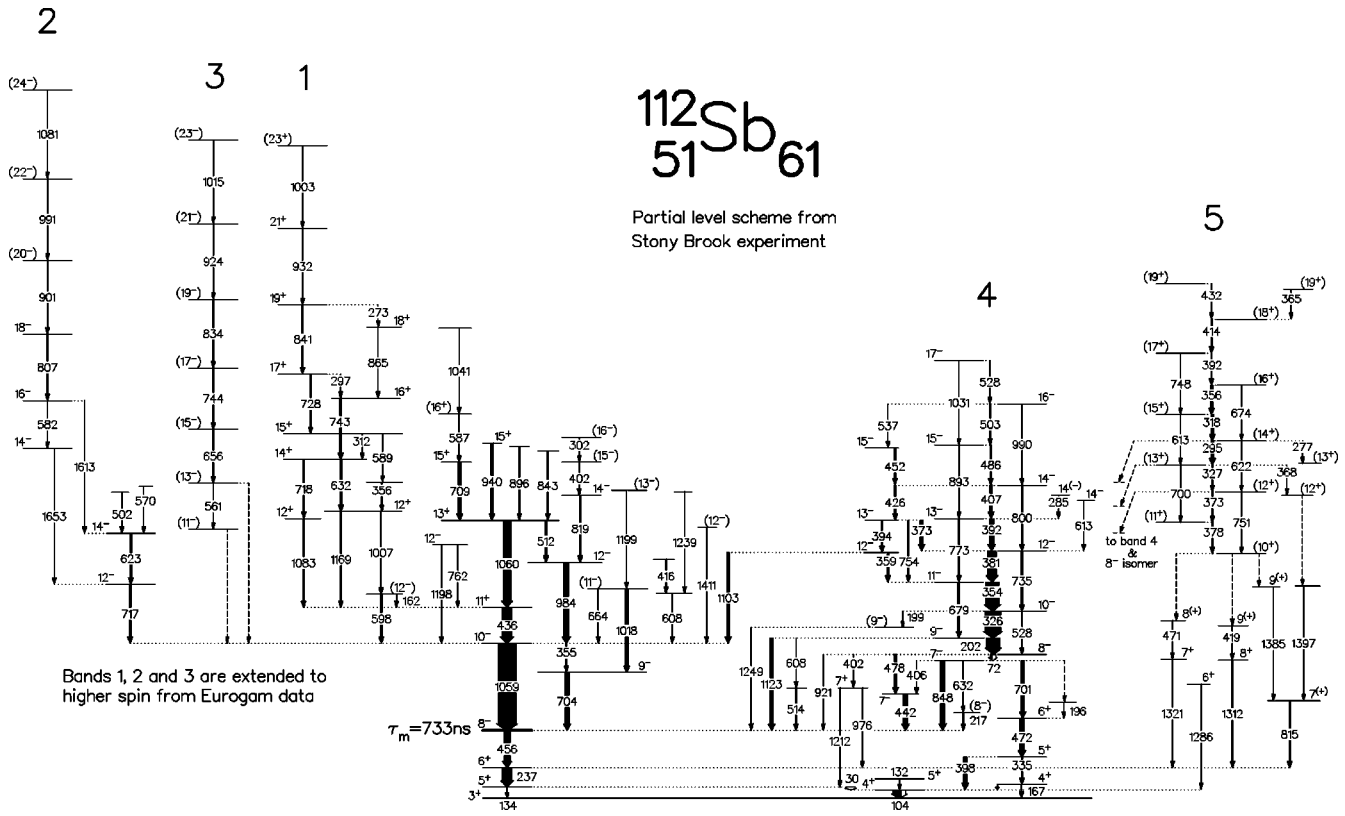

FIG. 1. Level scheme for ^{112}Sb deduced from the Stony Brook experiment. The widths of the transitions are proportional to their total intensity, with the white parts showing the calculated component from internal conversion. The anomalous intensity balance through the 8^- isomeric state reflects the observed loss of coincidence intensity due to the ± 159 ns coincidence overlap used in the Stony Brook experiment. Note that bands 1, 2, and 3 were extended to tentative spins of $39\hbar$, $38\hbar$, and $41\hbar$, respectively, in the Eurogam-II experiment (see Fig. 9). The dashed transitions represent unobserved decay paths (not necessarily single transitions) which are inferred from the coincidence relationships. The 4^+ levels at 167 and 104 keV are connected by such a dashed transition (see text), although the drawing scale makes this difficult to see. Note that the 30 keV, $5^+ \rightarrow 4^+$ transition is undashed, since it is believed to be a single discrete transition, although it was not observed directly in the present experiments.

coincidence data with γ rays producing single hits in any detector (coaxial or clover) on one axis and γ rays from scattering events in the clover detectors (clover double hits), which were either perpendicular or parallel to the reaction plane for the two matrices, on the other axis. Both matrices were single gated using the same gate list as in (ii) above so as to enhance the proportion of the most intense decoupled band in ^{112}Sb. The number of perpendicular, $N_\perp$, and parallel, $N_\parallel$, scatters for a given γ ray can be deduced by projecting out spectra gated by specific transitions on the single-hit axes. Assuming that all 96 separate clover elements have equal efficiencies, the linear polarization is given by

$$P = \frac{1}{Q}\frac{N_\perp - N_\parallel}{N_\perp + N_\parallel}, \tag{2}$$

where the polarization sensitivity Q for the clover detectors is taken from Ref. [29].

IV. RESULTS AND LEVEL SCHEME

The level scheme for ^{112}Sb obtained from the thick target experiment performed at Stony Brook is shown in Fig. 1, with the properties of the transitions assigned to ^{112}Sb presented in Table I. Note that, unless otherwise indicated, the following section refers to the results from the Stony Brook experiment. The level scheme in Fig. 1 can be roughly separated into two parts: (i) the two $\Delta I = 1$ bands known previously [26,27] and their decay towards the ground state and (ii) the high-spin states above the 8^- isomer which are new to this work, including the three decoupled bands. The different parts of the level scheme will be discussed separately in the following sections. First, however, a brief history will be given of prior studies of excited states in ^{112}Sb.

A. Prior results

There have been a number of prior studies of excited states in ^{112}Sb, dating back to the first low-spin investigations via ^{112}Te$\rightarrow^{112}$Sb decay [25] and using the (p,n) and $(^3\mathrm{He},xn)$ reactions [23]. The latter studies identified excited states up to $E_x = 1.17$ MeV, including the $I^\pi = 8^-$ isomer. Soon afterwards, an accurate half-life [32] as well as magnetic [33] and quadrupole [32] moments were measured for the $I^\pi = 8^-$ isomer. More recently, a comprehensive study of the low-spin states using the (p,n) reaction was performed by Fayez-Hassan *et al.* [24] and two high-spin studies were reported by Singh *et al.* [26] and Moon *et al.* [27]. The current high-spin study was performed in parallel with and independently of the more recent works and substantially confirms and in places changes their reported level schemes, based upon the new results presented here. Neither of the

TABLE I. Properties of transitions assigned to ^{112}Sb from the Stony Brook experiment.

E_γ[a] (keV)	I_γ[b]	$I_i^\pi \rightarrow I_f^\pi$	A_2[c]	R_{DCO}[d] 202/381	104/237	318	1059/1060	$M\lambda$
29.6	e	$5^+ \rightarrow 4^+$						$M1/E2$
72.4	11.7(4)	$8^- \rightarrow 7^-$		0.97(3)				$M1/E2$
103.9	45.2(18)	$4^+ \rightarrow 3^+$	−0.30(3)	0.86(2)			0.61(6)	$M1/E2$
132.5	1.37(16)	$5^+ \rightarrow 4^+$						$M1/E2$
133.5	1.68(7)	$5^+ \rightarrow 3^+$	0.18(5)		1.47(5)			$E2$
161.8	2.90(15)	$(12^-) \rightarrow 11^+$					0.67(11)	$(E1)$
167.1	4.4(15)	$4^+ \rightarrow 3^+$	−0.29(4)	0.98(9)				$M1/E2$
196.5	1.18(11)	$\rightarrow 6^+$						
199.3	2.22(13)	$10^- \rightarrow (9^-)$		1.33(24)				$(M1/E2)$
202.2	66(2)	$9^- \rightarrow 8^-$	-0.15(3)	0.96(2)	0.90(3)	0.86(5)		$M1/E2$
216.8	4.4(7)	$(8^-) \rightarrow 8^-$		1.52(12)				$(M1/E2)$
236.9	48.7(16)	$6^+ \rightarrow 5^+$	-0.18(3)	0.96(3)			0.55(2)	$M1/E2$
273.0	0.51(9)	$19^+ \rightarrow 18^+$					0.50(16)	$M1/E2$
277.2	3.04(16)	$(14^+) \rightarrow (13^+)$				1.02(9)	0.68(11)	$M1/E2$
285.2	3.94(16)	$14^{(-)} \rightarrow 13^-$		0.86(7)				$(M1/E2)$
294.9	16.1(5)	$(14^+) \rightarrow (13^+)$		0.88(3)		0.95(3)	0.51(5)	$M1/E2$
297.0	2.35(13)	$17^+ \rightarrow 16^+$					0.57(8)	$M1/E2$
302.0	1.28(18)	$(16^-) \rightarrow (15^-)$					0.76(7)	$(M1/E2)$
312.1	2.35(15)	$15^+ \rightarrow 14^+$					0.33(6)	$M1/E2$
317.8	14.2(5)	$(15^+) \rightarrow (14^+)$	-0.10(3)	0.96(8)			0.43(5)	$M1/E2$
325.5	85(3)	$10^- \rightarrow 9^-$	-0.05(3)	0.92(2)				$M1/E2$
326.8	5.1(2)	$(13^+) \rightarrow (12^+)$				0.96(4)		$M1/E2$
335.0	8.1(3)	$5^+ \rightarrow 4^+$		0.76(4)				$M1/E2$
353.9	71(2)	$11^- \rightarrow 10^-$	-0.06(3)	0.91(2)				$M1/E2$
355.2	4.9(2)	$10^- \rightarrow 9^-$	−0.03(3)[f]				0.40(5)	$M1/E2$
355.8	12.7(4)	$(16^+) \rightarrow (15^+)$	−0.03(3)[f]	0.99(12)		0.90(3)		$M1/E2$
356.2	4.0(4)	$\rightarrow (12^+)$	−0.03(3)[f]					
358.9	10.6(4)	$12^- \rightarrow 11^-$		0.79(3)				$M1/E2$
365.0	2.00(11)	$(19^+) \rightarrow (18^+)$				1.10(12)		$M1/E2$
368.2	0.66(5)	$(13^+) \rightarrow (12^+)$				1.26(25)		$(M1/E2)$
372.6	5.5(2)	$(12^+) \rightarrow (11^+)$				1.04(5)		$M1/E2$
373.5	16.4(5)	$13^- \rightarrow 12^-$		0.89(3)				$M1/E2$
378.2	6.0(3)	$(11^+) \rightarrow (10^+)$				1.09(17)		$M1/E2$
380.6	48.8(15)	$12^- \rightarrow 11^-$	−0.13(3)	0.94(2)		0.95(14)		$M1/E2$
391.6	6.8(3)	$(17^+) \rightarrow (16^+)$				0.90(4)	0.54(7)	$M1/E2$
392.4	25.2(8)	$13^- \rightarrow 12^-$		0.86(2)				$M1/E2$
394.4	7.5(3)	$13^- \rightarrow 12^-$					0.61(8)	$M1/E2$
398.2	19.2(7)	$5^+ \rightarrow 4^+$		0.63(2)		0.70(9)		$M1/E2$
402.0	2.91(13)	$8^- \rightarrow 7^+$		0.87(5)				$E1$
402.5	3.6(2)	$(15^-) \rightarrow 14^-$					0.28(7)	$(M1/E2)$
406.2	4.0(2)	$7^- \rightarrow 7^-$		1.14(4)[f]				$M1/E2$
406.9	13.6(4)	$14^- \rightarrow 13^-$		1.14(4)[f]				$M1/E2$
414.2	7.6(3)	$(18^+) \rightarrow (17^+)$		0.97(12)		0.91(5)		$M1/E2$
416.0	3.9(2)							
418.5	3.17(18)	$9^{(+)} \rightarrow 8^+$			0.91(6)			$(M1/E2)$
425.9	8.8(3)	$14^- \rightarrow 13^-$		1.10(6)			0.46(9)	$M1/E2$
432.5	3.15(13)	$(19^+) \rightarrow (18^+)$				0.91(8)		$M1/E2$
435.7	54.8(18)	$11^+ \rightarrow 10^-$	−0.25(3)			0.90(11)	0.49(2)	$E1$
441.9	24.9(14)	$7^- \rightarrow 8^-$		0.94(3)				$M1/E2$
451.9	6.3(2)	$15^- \rightarrow 14^-$		0.85(6)			0.32(6)	$M1/E2$
456.4	32.7(10)	$8^- \rightarrow 6^+$	0.28(3)				0.75(3)	$M2$
471.0	1.46(15)	$8^{(+)} \rightarrow 7^+$				0.84(7)		$(M1/E2)$
471.7	25.0(8)	$6^+ \rightarrow 5^+$	−0.17(3)	0.77(2)				$M1/E2$
478.5	13.7(5)	$8^- \rightarrow 7^-$	−0.45(5)	0.55(2)				$M1/E2$

TABLE I. (*Continued.*)

E_γ[a] (keV)	I_γ[b]	$I_i^\pi \rightarrow I_f^\pi$	A_2[c]	R_{DCO}[d] 202/381	104/237	318	1059/1060	$M\lambda$
486.3	6.7(2)	$15^- \rightarrow 14^-$		0.78(5)				$M1/E2$
501.6	3.17(16)	$\rightarrow 14^-$						
503.0	4.74(18)	$16^- \rightarrow 15^-$		0.87(7)				$M1/E2$
511.8	9.9(4)	$13^+ \rightarrow 12^-$						$E1$
513.9	7.2(10)	$\rightarrow 8^-$						
527.7	2.9(3)	$10^- \rightarrow 8^-$						$E2$
527.9	3.37(18)	$17^- \rightarrow 16^-$		0.75(6)				$M1/E2$
537.0	2.02(13)	$16^- \rightarrow 15^-$		0.86(8)				$M1/E2$
561.0	1.04(13)	$(13^-) \rightarrow (11^-)$						$(E2)$
570.1	1.93(13)	$\rightarrow 14^-$						
582.3	1.04(9)	$16^- \rightarrow 14^-$						$E2$
586.8	4.4(2)	$(16^+) \rightarrow 15^+$					0.16(8)	$(M1/E2)$
588.5	1.88(13)	$15^+ \rightarrow$						
597.5	10.2(6)	$(12^-) \rightarrow 10^-$					1.24(14)	$(E2)$
607.7	4.3(5)	$\rightarrow 10^-$						
607.9	1.48(18)	$9^- \rightarrow$						
613.0	0.13(11)	$(15^+) \rightarrow (13^+)$						$E2$
613.2	1.9(2)	$14^- \rightarrow 12^-$		1.51(14)				$E2$
621.7	0.73(11)	$(14^+) \rightarrow (12^+)$						$E2$
622.6	9.9(4)	$14^- \rightarrow 12^-$					1.01(14)	$E2$
631.6	2.99(15)	$7^- \rightarrow (8^-)$		0.94(14)				$(M1/E2)$
632.0	11.2(4)	$14^+ \rightarrow 12^+$					1.13(8)	$E2$
655.8	4.8(3)	$(15^-) \rightarrow (13^-)$						$(E2)$
664.0	2.7(5)	$(11^-) \rightarrow 10^-$					0.61(5)	$(M1/E2)$
673.9	0.89(11)	$(16^+) \rightarrow (14^+)$						$E2$
679.1	10.0(4)	$11^- \rightarrow 9^-$		1.71(8)				$E2$
699.7	1.11(7)	$(13^+) \rightarrow (11^+)$						$E2$
701.3	18.4(6)	$7^- \rightarrow 6^+$	0.10(2)	0.98(3)				$E1$
704.0	21.9(13)	$9^- \rightarrow 8^-$	$-0.58(5)$				0.39(9)	$M1/E2$
708.8	16.5(6)	$15^+ \rightarrow 13^+$					1.07(5)	$E2$
717.1	10.6(6)	$12^- \rightarrow 10^-$					0.92(6)[f]	$E2$
718.2	5.1(2)	$14^+ \rightarrow 12^+$					0.92(6)[f]	$E2$
727.7	3.32(16)	$17^+ \rightarrow 15^+$					1.35(18)	$E2$
734.6	9.2(4)	$12^- \rightarrow 10^-$		1.51(8)				$E2$
742.6	11.6(5)	$16^+ \rightarrow 14^+$					1.00(10)[f]	$E2$
743.7	5.7(3)	$(17^-) \rightarrow (15^-)$					1.00(10)[f]	$E2$
747.6	0.71(9)	$(17^+) \rightarrow (15^+)$						$E2$
750.6	2.31(11)	$(12^+) \rightarrow (10^+)$						$E2$
754.3	6.1(3)	$13^- \rightarrow 11^-$		1.39(10)				$E2$
761.9	2.1(2)	$12^- \rightarrow 11^+$						$E1$
773.5	6.0(3)	$13^- \rightarrow 11^-$		1.55(10)				$E2$
799.7	6.9(3)	$14^- \rightarrow 12^-$		1.43(9)				$E2$
806.5	4.7(7)	$18^- \rightarrow 16^-$					0.85(8)	$E2$
815.1	8.5(4)	$7^{(+)} \rightarrow 6^+$			0.56(3)	0.44(6)		$(M1/E2)$
818.6	9.2(4)	$14^- \rightarrow 12^-$					1.14(11)	$E2$
834.0	4.2(2)	$(19^-) \rightarrow (17^-)$					0.93(10)	$E2$
841.2	6.1(3)	$19^+ \rightarrow 17^+$					0.98(7)	$E2$
842.9	5.4(3)	$\rightarrow 13^+$						
848.4	22.8(8)	$7^- \rightarrow 8^-$	0.42(5)	1.39(5)				$M1/E2$
865.4	2.40(16)	$18^+ \rightarrow 16^+$					1.00(8)	$E2$
893.2	2.15(15)	$15^- \rightarrow 13^-$		2.1(5)				$E2$
896.4	3.1(2)	$\rightarrow 13^+$						
900.8	3.08(16)	$(20^-) \rightarrow 18^-$						$(E2)$

TABLE I. (*Continued.*)

E_γ[a] (keV)	I_γ[b]	$I_i^\pi \rightarrow I_f^\pi$	A_2[c]	R_{DCO}[d] 202/381	104/237	318	1059/1060	$M\lambda$
920.8	1.97(13)	$8^- \rightarrow 8^-$		1.44(17)				$M1/E2$
923.9	1.64(13)	$(21^-) \rightarrow (19^-)$						$(E2)$
932.2	3.26(18)	$21^+ \rightarrow 19^+$					0.98(16)	$E2$
940.1	12.0(5)	$15^+ \rightarrow 13^+$					1.09(7)	$E2$
976.0	4.4(2)	$7^+ \rightarrow 6^+$		0.56(6)				$M1/E2$
983.8	28.1(11)	$12^- \rightarrow 10^-$	0.41(5)				0.97(4)	$E2$
989.8	2.5(2)	$16^- \rightarrow 14^-$		1.62(9)				$E2$
990.8	1.8(9)	$(22^-) \rightarrow (20^-)$					0.91(7)	$E2$
1002.9	1.11(13)	$(23^+) \rightarrow 21^+$						$(E2)$
1007.4	6.2(3)	$12^+ \rightarrow (12^-)$					1.08(14)	$(E1)$
1015.3	1.58(13)	$(23^-) \rightarrow (21^-)$						$(E2)$
1017.6	14.2(6)	$(11^-) \rightarrow 9^-$	0.28(3)					$(E2)$
1030.8	<0.15	$17^- \rightarrow 15^-$						$E2$
1041.3	2.64(16)	$\rightarrow (16^+)$					0.79(8)	
1058.5	$\equiv 100.00$[a]	$10^- \rightarrow 8^-$	0.40(3)[f]		1.60(5)[f]	1.48(12)	1.01(2)[f]	$E2$
1060.0	43.1(14)	$13^+ \rightarrow 11^+$	0.40(3)[f]		1.60(5)[f]		1.01(2)[f]	$E2$
1080.6	0.20(9)	$(24^-) \rightarrow (22^-)$						$(E2)$
1083.0	6.7(3)	$12^+ \rightarrow 11^+$					0.54(3)	$M1/E2$
1103.4	16.1(8)	$12^- \rightarrow 10^-$			1.65(20)		1.02(7)	$E2$
1122.9	19.0(6)	$9^- \rightarrow 8^-$	0.37(5)	1.32(9)	1.34(10)			$M1/E2$
1168.8	6.7(3)	$12^+ \rightarrow 11^+$					0.47(5)	$M1/E2$
1197.7	5.9(5)	$12^- \rightarrow 10^-$					1.01(12)[f]	$E2$
1199.4	1.8(2)	$(13^-) \rightarrow (11^-)$					1.01(12)[f]	$(E2)$
1211.9	4.4(3)	$7^+ \rightarrow 5^+$		1.55(19)	1.95(16)			$E2$
1238.7	1.5(2)							
1249.1	4.1(8)	$(9^-) \rightarrow 8^-$		0.32(10)				$(M1/E2)$
1285.6	2.3(3)	$6^+ \rightarrow 4^+$			1.76(21)			$E2$
1312.3	6.1(3)	$8^+ \rightarrow 6^+$	0.7(3)		2.05(12)			$E2$
1321.3	2.7(2)	$7^+ \rightarrow 6^+$			0.69(6)			$M1/E2$
1385.5	1.15(13)	$9^{(+)} \rightarrow 7^{(+)}$	0.37(9)		2.19(41)			$E2$
1397.3	0.86(13)	$\rightarrow 7^{(+)}$	0.47(10)		1.25(13)			
1411.3	3.4(4)	$(12^-) \rightarrow 10^-$	0.40(9)				1.0(2)	$(E2)$
1613.2	3.9(2)	$16^- \rightarrow 14^-$	0.36(5)				1.01(16)	$E2$
1653.3	1.18(16)	$14^- \rightarrow 12^-$	0.4(1)				0.85(18)	$E2$

[a]Energies typically accurate to 0.2–0.3 keV, up to 1.0 keV for the weakest transitions.
[b]Coincidence γ-ray intensities relative to the 1058.5 keV transition.
[c]Anisotropies of intense uncontaminated transitions, deduced from angular projections of the coincidence data.
[d]DCO ratio gated by the marked transitions.
[e]Transition unobserved, but inferred from coincidence relationships.
[f]Result for composite peak.

two concurrent high-spin studies identified the states new to this work, which feed solely towards the long-lived isomer. The differences between the published level schemes are discussed in the following sections when appropriate.

B. $\Delta I = 1$ bands and their decay

1. States below the $I^\pi = 8^-$ isomer

The decay cascade from the $I^\pi = 8^-$ isomer to the ground state has had various interpretations [23,26,27,32,33], with the transitions in common to all interpretations having energies of 104, 237, and 456 keV. The current work confirms the existence of the 134 and 30 keV transitions deduced by Moon *et al.* [27] and observes a new 1212 keV transition which feeds the state at 133.5 keV, thereby conclusively demonstrating the placement of both the unobserved transition (energy of $133.5 - 103.9 = 29.6$ keV) and the 133.5 keV transition. It is interesting that the state at 133.5 keV (and its associated γ-ray decay) was not observed in the sensitive (p,n) experiment by Fayez-Hassan *et al.* [24]. They did, however, observe a γ ray with an energy of 132.6 keV which they placed directly feeding the state at $E_x = 104$ keV. This is confirmed by the current results since a γ ray with an energy of 132.5 keV is found to be in coincidence with the 104 keV transition.

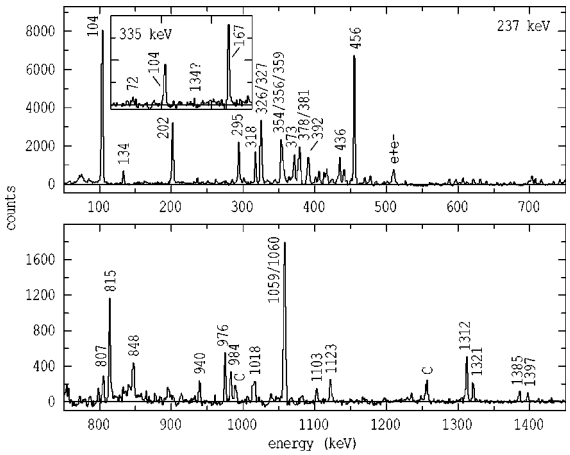

FIG. 2. Low- and high-energy regions of the coincidence spectrum for the 237 keV transition in ^{112}Sb. Contaminant γ rays from ^{112}Sn are marked by the letter C. The inset in the upper panel is the low-energy region of the 335 keV coincidence spectrum to be compared with the same region of the 237 keV spectrum as described in the text.

The other major difference with Ref. [24] is related to this problem and concerns the placement of the 236.9 keV transition (see Fig. 2). The authors of Ref. [24] observe a transition with this energy to be in coincidence with the 103.9 keV transition, but tentatively place it as feeding a level at 129.6 keV, which then decays to the 103.9 keV level. From the current work, the presence of the 976/237 keV cascade and its associated 1212 keV crossover transition unambiguously places the 236.9 keV transition as instead feeding the state at 133.5 keV.

Reference [24] suggests that the 4^+ state at 167.1 keV decays both to the ground state and also via a two-step cascade of low-energy transitions (37.5 and 25.8 keV), passing through their proposed state at 129.6 keV and then to the 103.9 keV state. The current work confirms the existence of a decay path similar to that postulated above, via the observation of coincidences between the 335.0 keV transition and both the 167.1 and 103.9 keV transitions (see the inset in Fig. 2). It is possible, however, that the 37.5/25.8 keV cascade proposed in Ref. [24] should be replaced by a 33.6/29.6 keV cascade via the 133.5 keV level which was observed in the current work. Unfortunately, the current data are not sensitive to transitions of this low energy. However, the inset in Fig. 2 shows the 100–130 keV energy region from the coincidence spectrum for the 335.0 keV transition. The relative peak heights of the 103.9 and (possibly) 133.5 keV γ rays should reproduce those observed in the 237 keV spectrum, were the 33.6/29.6 keV cascade to occur. The statistics is not sufficient to be able to distinguish this, which leaves the question of which cascade is correct unanswered. The current level scheme in Fig. 1 shows only an unobserved decay path leading from the level at 167.1 keV to that at 103.9 keV and does not pass judgement on whether it might be a two-step cascade via the level at 133.5 keV, with this level effectively replacing that proposed at 129.6 keV by Ref. [24]. Note that the alternative proposed states have the same assigned spin and parity and differ by only 4 keV in excitation energy.

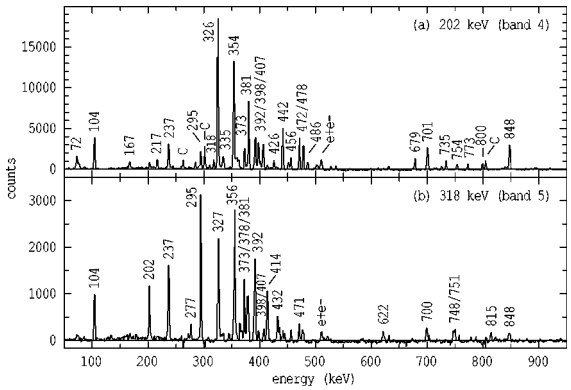

FIG. 3. Coincidence spectra for (a) the 202 keV transition from band 4 and (b) the 318 keV transition from band 5. Known contaminant γ rays are marked by the letter C.

2. Band 4

The band labeled 4 in Fig. 1 carries approximately 30% of the ^{112}Sb channel intensity and was observed by both Singh *et al.* [26] and Moon *et al.* [27]. Other than the different placements for the unobserved 30 keV transition, the decay schemes of both these previous works for band 4 and its decay towards the ground state are similar. Figure 3(a) shows the coincidence spectrum from the current work for the 202 keV transition in band 4. The previous placements of the decay-out transitions are confirmed, while a number of new transitions with energies of 608, 514, 402, 976, 1212, 632, 217, 199, 1249, and 196 keV are observed. At higher spin within band 4 the 373, 360, 402 keV cascade placed by Moon *et al.* is not observed. However, their placement of the side transitions feeding into and out of the band between the 16^- and 11^- levels is confirmed. In addition, the current level scheme contains the newly observed 394 and 359 keV transitions (with the corroborating 1103 keV transition towards the 8^- isomer) as well as the 285 and 613 keV transitions feeding into the band.

The spins and parities of the levels discussed so far have been assigned using the following methodology. The comprehensive study by Fayez-Hassan *et al.* [24] using Hauser-Feshbach analysis as well as angular distribution measurements has already established the spins and parities of the low-spin states. These results constitute the base upon which the current level scheme is built. The results of the current angular distribution analysis for the intense, uncontaminated transitions in ^{112}Sb are presented in Table I. Where there is an overlap with Ref. [24], the positive/negative values for A_2, indicating stretched quadrupole/dipole transitions, are in agreement with the previous multipolarity assignments. DCO ratios were also employed to ascertain the multipolarities of the weaker transitions for which an angular distribution analysis was impossible. To do this, the assumption was made that band 4 consists of $M1$ transitions with $E2$ crossovers. This is supported by the fact that the in-band cascade transitions from band 4 (202, 326, 354, and 381 keV) all have negative A_2 coefficients, indicating stretched dipole assignments which are almost certainly $M1/E2$ due to the presence of competing crossover ($E2$) transitions. These assumptions allowed the DCO ratios of the 202 and 381 keV transitions to be determined by gating on the $E2$ crossover transitions, giving averaged results of 0.637(16) and

TABLE II. Calculated DCO ratios (for the Stony Brook detector geometry) for different types of transitions using a stretched quadrupole as the gating transition.

Multipolarity	$I_i \rightarrow I_f$	R_{DCO}
Quadrupole	$I \rightarrow I-2$	1.00
Quadrupole	$I \rightarrow I-1$	0.66
Quadrupole	$I \rightarrow I$	0.50
Dipole	$I \rightarrow I-1$	0.54
Dipole	$I \rightarrow I$	1.05
Dipole	$I \rightarrow I+1$	0.58
Dipole/quadrupole ($\delta<0$)	$I \rightarrow I-1$	<0.54
Dipole/quadrupole ($\delta>0$)	$I \rightarrow I-1$	>0.54

0.668(29), respectively. These values can be compared with the expected DCO ratios for the Stony Brook array which are presented in Table II and were calculated using the methods of Ref. [31] assuming an m-substate distribution with $\sigma/I = 0.3$. Results are presented for a variety of transitions gated by a pure, stretched quadrupole transition. From the table it can be seen that the 202 and 381 keV transitions have positive mixing ratios; a complete calculation (not presented here) gives $\delta = 0.094(14)$ and $\delta = 0.120(25)$ for the 202 and 381 keV transitions, respectively. Table III presents further calculations showing the expected DCO ratios for the Stony Brook array using a mixed $M1/E2$ transition with $\delta = 0.094$ as the gating transition (cf. 202 keV transition). The DCO calculations can be confirmed by using the 202 keV transition as a gate to determine experimental DCO ratios (and hence multipolarities and the signs of the mixing ratios) for the low-spin transitions. These results are in good agreement with the assignments of Fayez-Hassan *et al.* [24]. Thus, the calculations in Tables II and III can be used to understand the complex decay from the bottom of band 4 towards the 8^- isomer and the ground state.

There are systematic observations of rotational bands with $9^- \rightarrow 8^-$ transitions having energies around 200 keV in all the odd-odd antimony isotopes from $A=108$ to $A=120$ [10,26,27,34–39]. Moon *et al.* [27] assign the 202 keV transition in ^{112}Sb to be $10^- \rightarrow 9^-$ on the basis of an $E2$ character for the 1123 keV transition, while commenting on the disagreement of this assignment with systematics. Singh *et al.* [26] assign the transition in agreement with systematics, but then leave a 30 keV energy gap in the decay of the band towards the isomer so as to obtain the correct spin assignment. The current spins are in agreement with the systematics and are also supported by the DCO ratios gated by the 202 and 381 keV transitions in the following way.

TABLE III. Calculated DCO ratios (for the Stony Brook detector geometry) for different types of transitions using a stretched dipole/quadrupole ($\delta = 0.094$) as the gating transition.

Multipolarity	$I_i \rightarrow I_f$	R_{DCO}
Quadrupole	$I \rightarrow I-2$	1.52
Quadrupole	$I \rightarrow I-1$	0.91
Quadrupole	$I \rightarrow I$	0.89
Dipole	$I \rightarrow I-1$	0.86
Dipole	$I \rightarrow I$	1.60
Dipole/quadrupole ($\delta<0$)	$I \rightarrow I-1$	<0.86
Dipole/quadrupole ($\delta>0$)	$I \rightarrow I-1$	>0.86

The DCO ratios for the 402, 976, 1212 keV set of γ rays suggests that they are pure dipole ($E1$), mixed dipole/quadrupole ($M1/E2$) and stretched quadrupole ($E2$) transitions, respectively, leading to the spin and parity assignments shown. The 921 keV transition has a DCO ratio in agreement with a $\Delta I=0$, $M1/E2$ transition. The 632, 217 keV cascade is in agreement with expectations for an $I \rightarrow I+1$, $M1/E2$ and $\Delta I=0$, $M1/E2$ cascade. The 478, 442 keV path is in agreement with a cascade of two stretched $M1/E2$ transitions (the 406 keV transition lies close in energy to the more intense 407 keV in-band transition, and so its DCO ratio could not be determined.) The 199, 1249 keV cascade is consistent with both transitions being stretched $M1/E2$ transitions, although the DCO ratio for the 199 keV γ ray has a large error. All the above assignments are consistent with the 202 keV transition having a $9^- \rightarrow 8^-$ assignment. The 608, 514 keV cascade was too weak and/or contaminated to measure the DCO ratios. Three of the other transitions decaying out of band 4 have ambiguities with respect to the assigned spins and/or parities, as discussed in the next two paragraphs.

Results from the current work agree with the prior assignment [24,26,27] of $I^\pi = 5^+$ to the level from which the 398 and 335 keV transitions decay. The DCO ratio and angular distribution for the 472 keV transition suggests it is a stretched dipole transition with a negative mixing ratio ($M1/E2$) so that it decays from a 6^+ level. Since the 72 keV transition appears to have the same character as the 202 keV in-band transition and fits well into the energy systematics [10,26,27,34–39], it has been assigned as the $8^- \rightarrow 7^-$ transition. This implies that the 701 keV transition must be a stretched $E1$, $7^- \rightarrow 6^+$ transition; however, its DCO ratio gated by the 202 keV γ ray suggests that it is a stretched dipole transition with a small positive mixing ratio, implying $M1/E2$ character. This discrepancy is probably due to slight contamination from a transition in the other strongly populated channel, ^{112}Sn. Note that changing the character of the 701 keV transition to $M1/E2$ would not affect the $9 \rightarrow 8$ spin assignment for the 202 keV transition.

Two other transitions do not obviously agree with the present spin assignments. The 1123 keV transition should be a stretched $M1/E2$ transition ($R_{\mathrm{DCO}} \approx 0.86$); however, its DCO ratio is 1.32(9). And the 848 keV transition should be an $I \rightarrow I+1$, $M1/E2$ transition ($R_{\mathrm{DCO}} \approx 0.90$); however its DCO ratio is 1.39(5). A possible explanation is that both of these transitions have $E2$ admixtures with $\delta \sim +1$, giving rise to the large DCO values. This is perhaps expected since both transitions decay directly from levels in band 4 to the 8^- isomer, with these levels corresponding to $\pi g_{9/2} \otimes \nu h_{11/2}$ and $\pi d_{5/2} \otimes \nu h_{11/2}$ single-particle structures, respectively (see Sec. V). Thus the decay can proceed via a $\pi g_{9/2} \rightarrow \pi d_{5/2}$ transition. Were this to be the case, it might be expected to also see a $10^- \rightarrow 8^-$ transition, but this is not observed. This is consistent with previous observations of the decay of the equivalent of band 4 to the 8^- isomer in many of the odd-odd antimony isotopes. While transitions from the 9^-, 8^-, and 7^- in-band levels to the 8^- isomer are observed in nearly all cases [10,26,27,34–39], there are no

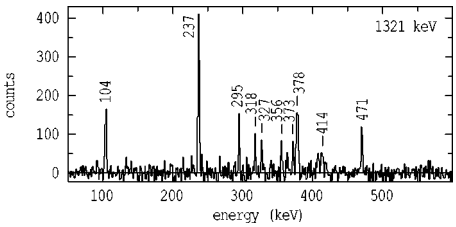

FIG. 4. Coincidence spectrum for the 1321 keV transition in ^{112}Sb, illustrating the decay path from band 5 directly towards the ground state which bypasses band 4 and the 8^- isomer.

cases where the 10^- in-band level is observed to decay to the 8^- isomer.

3. Band 5

A coincidence spectrum for the 318 keV transition from band 5 is shown in Fig. 3(b). This structure carries approximately 6% of the ^{112}Sb channel intensity and was known from both of the recent high-spin studies, albeit with very different placements of the band in the level scheme [26,27]. Observing the transitions linking band 5 to the rest of the level scheme was complicated by the unfortunate fact that the strongest transitions resulting from Coulomb excitation of the ^{103}Rh target (294.9 and 357.3 keV) coincided closely in energy with transitions in band 5. Also, bands 4 and 5 have a number of common transitions with very close energies. These problems meant that the current work did not have sufficient sensitivity to succeed in connecting band 5 into the rest of the level scheme. The dotted arrows in Fig. 1 indicate the unobserved decay paths suggested by the coincidence relationships. Part of the decay of the band proceeds towards the group of high-energy transitions in the lower right of the level scheme. That these high-energy transitions feed the very lowest positive-parity states is certain from the coincidence relationships with the 104 and 237 keV transitions (see Figs. 2 and 4). The assigned spins and parities of the levels follow from DCO ratios obtained by gating upon the 104 and 237 keV transitions. Since both of these transitions have almost pure dipole character [24], the expected DCO ratio (using the 104 and 237 keV transitions as gates) for a stretched quadrupole transition can be obtained from Table II as $1/0.54=1.85$, while by definition it will be 1.00 for a pure stretched dipole transition. Figure 4 shows the coincidence spectrum for the 1321 keV transition and confirms the existence of a decay path from band 5 towards the 471, 1321, 237, 30, 104 keV cascade. Note that the coincidence spectrum for the 237 keV transition in Fig. 2 shows transitions from band 5 as intensely as those from band 4. This is because band 5 feeds the 6^+ level at 370 keV mostly by decay paths around the isomer as shown on the right of Fig. 1, whereas band 4 feeds the 6^+ level mostly through the 8^- isomer. (The γ-ray coincidence overlap being shorter than the lifetime of the isomer attenuates the coincidences across the isomeric state.) This intensity relationship suggests that the placement by Singh *et al.* [26] of band 5 solely feeding band 4 must be incorrect. The alternative placement by Moon *et al.* [27] of band 5 feeding both the 8^- isomer and the 6^+ state at 370 keV can be ruled out, for example, by the 1321 keV coincidence spectrum in Fig. 4; the inferred

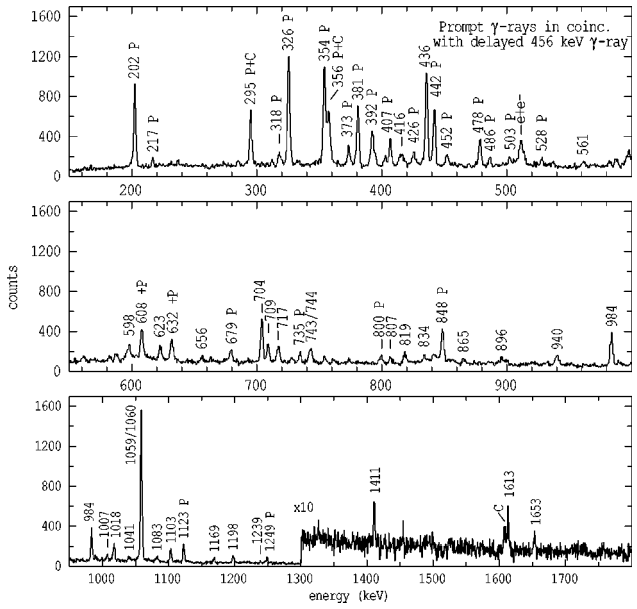

FIG. 5. Prompt γ-ray spectrum in coincidence with the time-delayed 456 keV transition which depopulates the 8^- isomer. Transitions from the decay of bands 4 and 5 are marked with the letter P. The 295 and 356 keV transitions are partly due to bands 4 and 5, but are also marked with the letter C to indicate they have a contaminant component (in this case from Coulomb excitation of the target). The other labeled γ rays are newly assigned as transitions which feed towards the 8^- isomer. Note that the top two panels show only a 450 keV energy region as compared to the bottom panel which shows an 850 keV energy region.

decay cascade shows clearly that band 5 must lie higher in excitation energy than Moon *et al.* suggest.

There is a loss of transition intensity at low spin in band 5 which indicates that the decay out of the band occurs over a number of transitions in a fragmented fashion, possibly another reason why discrete links were not observed. Various coincidence spectra [see Fig. 3(b), for example] show that the 318 keV transition in band 5 is in coincidence with transitions in band 4 up to at least the 407 keV, $14^-\rightarrow 13^-$ transition. Estimates from various coincidence spectra imply that approximately 20%, 40%, and 40% of the intensity in band 5 feeds towards the 8^- isomer, band 4, and the low-spin positive-parity states, respectively. This evidence, plus the observed feeding into levels with spins up to $9\hbar$, suggests that the spin of the bottommost level must be at least $9\hbar$, and is most likely $\geqslant 10\hbar$. Positive parity is assumed for the band consistent with the expected configuration discussed in Sec. V.

C. Decoupled bands and states above the 8^- isomer

Figure 5 shows a spectrum of γ rays observed prompt with respect to the beam pulse and in coincidence with the time-delayed 456 keV γ ray which depopulates the 8^- isomer. The transitions marked with the letter P correspond to γ rays which were either known previously or have been associated with the decay out of bands 4 and 5 from the current work. All the other labeled γ rays are observed for the first time and feed eventually towards the 8^- isomer as shown in the left-hand part of Fig. 1. Since the strongest transitions

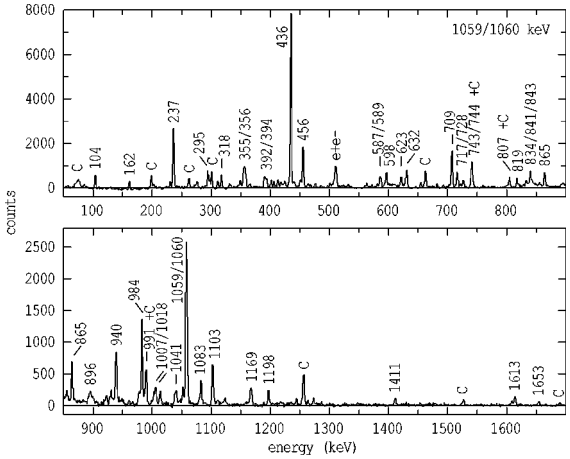

FIG. 6. Coincidence spectrum for the complex 1059/1060 keV doublet in ^{112}Sb. Known contaminant γ rays are marked with the letter C.

present in the isomer-feeding spectrum (Fig. 5) are the 1059/1060 keV doublet and the 436 keV transition, they have been assigned as a cascade feeding directly into the isomer. The placement of the 1059 keV transition as lowest is confirmed both by intensity measurements and the existence of the 1103 keV transition which feeds across from band 4. The coincidence spectrum for the 1059/1060 keV doublet shown in Fig. 6 illustrates most of the newly assigned γ rays. Angular distributions for the 1059/1060 keV doublet and the 436 keV transition suggest that they are stretched quadrupoles (assumed $E2$) and a stretched dipole, respectively. Since virtually all of the newly observed transitions above the 8^- isomer are in coincidence with at least one of the members of the 1059/1060 keV doublet, it is possible to use DCO ratios gated by these stretched $E2$ transitions to assign transition multipolarities. Where available, the DCO results are in agreement with the angular distribution data.

To determine the spins and parities fully it is necessary to ascertain the electric or magnetic character of the 436 keV transition. It has a DCO ratio close to that expected for a pure stretched dipole transition and has been assigned $E1$ character. This agrees with both the systematics of the neighboring odd-odd antimony isotopes [10,36,37] and with the polarization measurements to be discussed below. Following these basic assignments, the irregularly spaced spherical states which decay into the 1060-436-1059 ($E2$-$E1$-$E2$) cascade can have their spins and parities assigned from the DCO ratios.

At the highest limits of the spin input into the reaction, the beginnings of rotational, stretched $E2$ cascades are observed. The lowest transitions of band 1 (populated with approximately 2.0% of the total channel intensity) and its associated decay can be seen in the coincidence spectrum for the 728 keV transition in Fig. 7(a). The rather complicated decay path below the band is clearly defined by both coincidence relationships and the energy sums of crossover transitions. The spins and parities of the states follow from the DCO ratios assuming stretched transitions for all but the 1007 keV transition. This is because both the 1007 and 598 keV transitions have DCO ratios indicative of stretched $E2$ character, while the 162 keV transition looks like a stretched dipole. The only way in which these results can be reconciled with

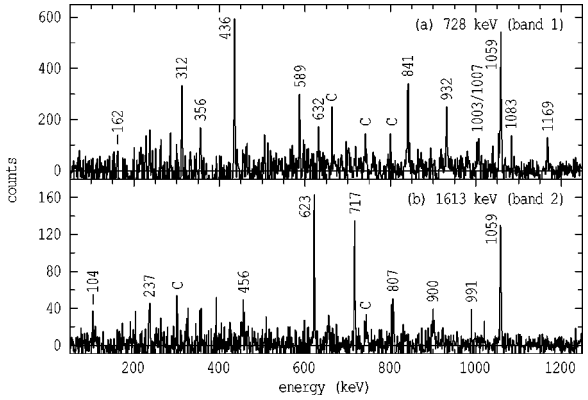

FIG. 7. (a) Coincidence spectrum for the 728 keV transition linking band 1 to the low-spin levels. The spectrum has been deconvolved from nearby contaminant peaks due to ^{112}Sn. Some contaminants remain and are marked with the letter C. (b) Similar to (a) except for the 1613 keV transition linking band 2 to the low-spin levels.

one another is if the 1007 keV transition is in fact a $I \rightarrow I$ transition. Furthermore, the 162 keV transition must have $E1$ character or else the 598 keV transition would be $M2$. This is in agreement with the DCO ratio of the 162 keV transition, considering the reasonably large error bar.

Band 1 could be extended to high spin using the results from the thin-target Eurogam-II experiment. Figure 8(a) shows a sum of coincidence spectra from the $\gamma\gamma\gamma$ coincidence cube, double gated on combinations of the 1059 keV transition with the in-band transitions from 932 to 1871 keV. The extension of band 1 to higher spins is obvious. Note that there is a 1059 keV transition within the band which has nearly the same energy as the lower-spin 1059 and 1060 keV transitions. This was evident from the coincidence relation-

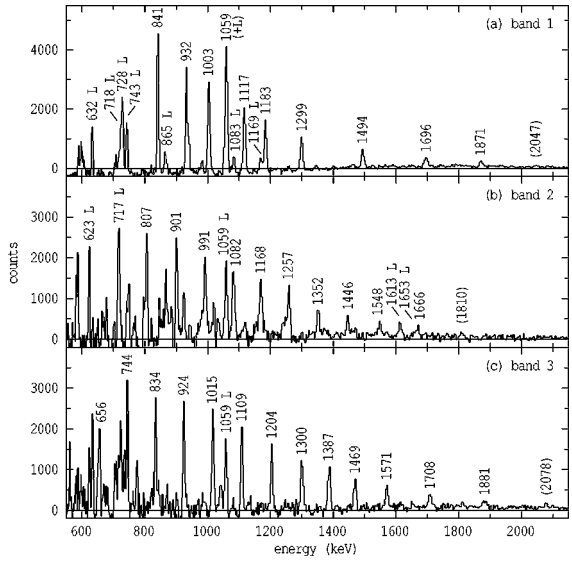

FIG. 8. Coincidence spectra for bands 1, 2, and 3 from the $\gamma\gamma\gamma$-coincidence cube created from the Eurogam-II data. The spectra are sums of double gates on in-band transition members. The bands are only very weakly populated, and so to obtain adequate statistics to illustrate the bands, some gates are chosen that introduce a number of unavoidable (unmarked) contaminants. Transitions linking towards the 8^- isomer are marked with the letter L.

TABLE IV. Properties of transitions associated with bands 1, 2, and 3 in ^{112}Sb as deduced from the Eurogam-II experiment.

Band 1				Band 2			Band 3		
E_γ (keV)	I_γ[a]	$I_i^\pi \rightarrow I_f^\pi$	R_{DCO}	E_γ (keV)	I_γ[a]	$I_i^\pi \rightarrow I_f^\pi$	E_γ (keV)	I_γ[a]	$I_i^\pi \rightarrow I_f^\pi$
841.3(1)	≡100	$19^+ \rightarrow 17^+$	0.97(5)	806.0(3)	66(5)	$18^- \rightarrow 16^-$	655.7(4)	68(10)	$(15^-) \rightarrow (13^-)$
932.0(2)	96(6)	$21^+ \rightarrow 19^+$	1.21(11)	901.2(3)	76(5)	$(20^-) \rightarrow 18^-$	743.8(2)	97(6)	$(17^-) \rightarrow (15^-)$
1002.8(3)	89(8)	$23^+ \rightarrow 21^+$	0.98(7)	991.3(3)	81(5)	$(22^-) \rightarrow (20^-)$	833.4(2)	91(6)	$(19^-) \rightarrow (17^-)$
1059.0(5)	87(9)	$25^+ \rightarrow 23^+$	0.99(5)	1081.5(3)	82(5)	$(24^-) \rightarrow (22^-)$	923.6(2)	91(6)	$(21^-) \rightarrow (19^-)$
1116.8(2)	81(4)	$27^+ \rightarrow 25^+$	1.27(20)	1168.3(3)	78(6)	$(26^-) \rightarrow (24^-)$	1016.1(2)	86(5)	$(23^-) \rightarrow (21^-)$
1183.2(2)	58(4)	$29^+ \rightarrow 27^+$	1.23(32)	1257.0(4)	64(5)	$(28^-) \rightarrow (26^-)$	1108.9(2)	80(6)	$(25^-) \rightarrow (23^-)$
1298.8(2)	49(3)	$31^+ \rightarrow 29^+$	1.06(22)	1352.4(4)	35(4)	$(30^-) \rightarrow (28^-)$	1203.9(3)	72(5)	$(27^-) \rightarrow (25^-)$
1493.6(3)	32(2)	$33^+ \rightarrow 31^+$	0.83(27)	1445.8(5)	29(3)	$(32^-) \rightarrow (30^-)$	1299.8(3)	67(5)	$(29^-) \rightarrow (27^-)$
1695.5(3)	26(2)	$(35^+) \rightarrow 33^+$		1548.2(6)	25(3)	$(34^-) \rightarrow (32^-)$	1387.0(3)	61(4)	$(31^-) \rightarrow (29^-)$
1871.3(5)	16(2)	$(37^+) \rightarrow (35^+)$		1666.0(7)	21(2)	$(36^-) \rightarrow (34^-)$	1468.6(3)	37(3)	$(33^-) \rightarrow (31^-)$
(2047)	6(1)	$(39^+) \rightarrow (37^+)$		(1810)	14(2)	$(38^-) \rightarrow (36^-)$	1570.6(4)	33(3)	$(35^-) \rightarrow (33^-)$
							1708.0(5)	16(2)	$(37^-) \rightarrow (35^-)$
							1880.8(7)	11(2)	$(39^-) \rightarrow (37^-)$
							(2078)	5(2)	$(41^-) \rightarrow (39^-)$

[a]Normalized to $I_\gamma = 100$ for the 841.3 keV transition in band 1.

ships and intensities obtained from the individual double-gated spectra. The presence of the 1059 keV transition in the band and the fact that in the data set this transition was predominantly due to the 1059/1059/1060 keV transitions in ^{112}Sb meant that it was possible to create gated coincidence matrices with an enhanced proportion of events corresponding to the decay of band 1. This is because the inclusion of the 1059 keV transition in the gate list strongly enhanced the band since the 1059 keV transition was in dual coincidence with every other transition in the band. Using the gated DCO matrix described in Sec. III it was possible to measure the DCO ratios of the in-band transitions up to the 1494 keV transition, verifying that they have stretched quadrupole character. The properties of the extra transitions assigned to band 1 from the Eurogam-II experiment are summarized in Table IV. Although they are not presented in Table IV, the DCO ratios which were obtained from the gated matrix for the low-spin transitions beneath band 1 were in agreement with the results from the Stony Brook experiment. Note that the intensities of the transitions for the decoupled bands were extremely difficult to measure due to their weak population in the Eurogam-II experiment; thus, the ordering of the transitions relies, at least in part, on the expectation of increasing transition energy with spin.

Matrices gated by transitions from band 1 were also created from events which had double hits occurring in the clover detectors. These matrices were used to extract polarization information as described in Sec. III. The results are presented in Table V and are in agreement with the multipolarity assignments from the DCO ratios. Measurements for low-energy transitions are difficult due to the small probability for Compton scattering of a low-energy γ ray from one element of a clover Ge crystal to another. Thus, no measurement could be made to confirm whether the 162 keV γ ray was an $E1$ transition. Nevertheless, the results confirm that the 436 keV transition has electric character and therefore firmly establish the parity of band 1.

Bands 2 and 3 were populated with slightly less intensity than band 1, comprising approximately 1.6% and 1.9% of the total channel intensity, respectively. Only band 2 could be linked into the low-spin-level scheme. Its decay is somewhat simpler than that of band 1 as illustrated in the level scheme shown in Fig. 1 and demonstrated experimentally in Fig. 7(b), where the coincidence spectrum for the 1613 keV linking transition is shown. The spin and parity of band 2 follow from the stretched $E2$ character of the linking transitions as determined from the Stony Brook DCO measurements. These linking transitions can also be seen in Fig. 8(b) which shows the extension of band 2 to high spin using the thin-target data. Although band 3 was not linked to the low-spin-level scheme, it too was extended to high spin using the

TABLE V. Linear polarizations of transitions associated with band 1 in ^{112}Sb and its decay.

E_γ (keV)	P	$M\lambda$[a]
273	−0.3(3)	$M1/E2$
297	−0.15(20)	$M1/E2$
312	−0.5(2)	$M1/E2$
436	0.19(7)	$E1$
718	0.12(19)	$E2$
728	0.55(10)	$E2$
743	0.21(18)	$E2$
841	0.41(8)	$E2$
865	0.2(3)	$E2$
931	0.67(11)	$E2$
1003	0.52(11)	$E2$
1059[b]	0.46(11)	$E2$
1083	−0.3(3)	$M1/E2$
1117	0.76(18)	$E2$
1183	0.6(3)	$E2$
1299	0.3(3)	$E2$

[a]$M\lambda$ deduced from results in Tables I and IV as well as the polarization results in this table.

[b]Composite peak (1059, 1060, and 1059 keV).

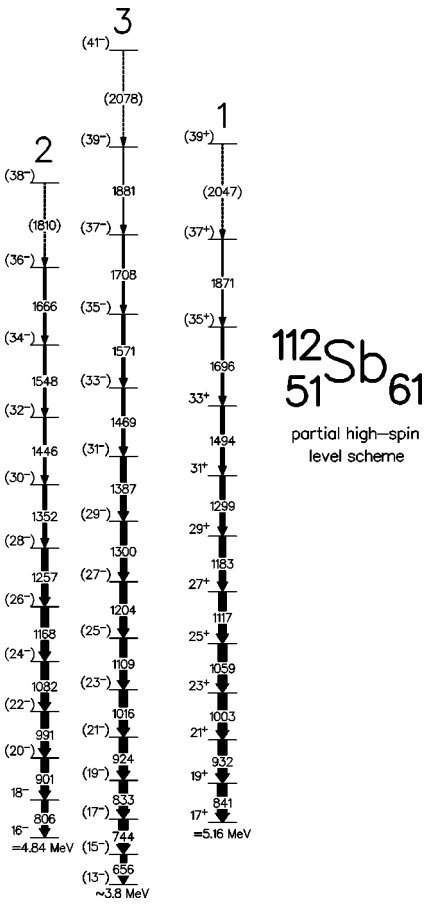

FIG. 9. Simplified high-spin level scheme for ^{112}Sb showing the extensions of the decoupled bands 1, 2, and 3 as deduced from the thin-target, Eurogam-II experiment.

thin-target data as shown in Fig. 8(c). Without the equivalent of the fortuitous 1059/1059/1060 keV coincidences found for band 1, it was difficult to enhance the population of bands 2 and 3 in gated matrices from the thin-target data. Thus, the high-spin transitions in bands 2 and 3 have assumed $E2$ character, with the γ-ray energies and level placements summarized in Table IV. The spins, parity, and approximate excitation energy of band 3 were determined by constraining it to be the signature partner of band 2 at low spin. (Theoretical reasons for this are outlined in Sec. V.) The coincidence relationships between the transitions in band 3 and the 1059 keV, $10^- \rightarrow 8^-$ transition result in the suggested decay paths indicated by the dashed arrows. These are in good agreement with expectations if band 3 is indeed the signature partner of band 2. Note, finally, that the extensions of bands 1, 2, and 3 to high spin are summarized in the simplified high-spin level scheme for ^{112}Sb in Fig. 9.

V. DISCUSSION

The excited states in ^{112}Sb can be characterized in terms of the number of protons excited across the $Z=50$ closed shell. Shell-model excitations predominate at low spin and excitation energy, while, at slightly higher excitation energy, the $\pi g_{7/2}$-$\pi g_{9/2}$ level crossing at $\beta_2 \approx 0.2$ governs the nuclear shape, since proton particle-hole excitations between these two levels can drive the nucleus to prolate deformation. A 1p-1h proton excitation leaves one high-K hole in the $\pi g_{9/2}$ shell and gives rise to strongly coupled structures like bands 4 and 5. A 2p-2h proton excitation results in two high-K $\pi g_{9/2}$ holes, leading to decoupled structures like bands 1, 2, and 3. The following section discusses these three different types of structure separately. First, however, some brief points are made concerning the measured γ-ray coincidence intensities.

A. Intensities and side feeding

The intensities listed in Table I and shown graphically in Fig. 1 represent γ-ray coincidence intensities obtained by fitting the coincidence matrix gated by the multiplicity condition $K \geqslant 1$. Because of the implicit ± 159 ns γ-ray coincidence overlap, this implies that a proportion of the coincidences between transitions above and below the long-lived 8^- isomer is not measured. This results in the anomalous intensity balance at the 8^- level with apparently more intensity feeding in than decaying out. The ratio of the measured coincidence intensity feeding out of and into the 8^- level is ~ 0.14, which, when combined with the ± 159 ns coincidence overlap, implies a mean lifetime for the $I^\pi = 8^-$ isomer of ~ 1 μs. Considering the crudeness of this measurement, this is surprisingly good agreement with the known lifetime of 733(32) ns [32]. It is also worth explicitly pointing out that the individual γ-ray intensities are given relative to that for the 1059 keV, $10^- \rightarrow 8^-$ transition and are not percentages of the total channel intensity. Summing the various decay paths to the ground state and allowing for the losses across the isomer, the total intensity of the ^{112}Sb channel is approximately 300 in the units of Table I.

A careful examination will reveal that there are ambiguities in the feeding intensities for some of the states in ^{112}Sb. For example, of the five 12^- states placed in the level scheme, some of the more yrast 12^- states appear to be populated less strongly than the more nonyrast states. The explanation for this may lie in the fact that the excited states in ^{112}Sb represent a range of different shapes and structures ranging from prolate deformed 1p-1h and 2p-2h proton excitations to near-spherical, shell-model excitations. Some selective feeding may be involved depending upon what path the system follows during deexcitation from the compound nucleus. Furthermore, in an odd-odd nucleus with high level density there is a potential for missed transitions and unplaced intensity.

B. Shell-model excitations

The low-energy, low-spin spherical states have been studied previously using (p,n) and $(^3\mathrm{He},xn)$ reactions [23,24]. For a complete summary of these lowest states, including those not observed in the current heavy-ion experiments, the reader is referred to the work of Ref. [24], which classifies the states using the Paar parabolic rule to describe the couplings of the unpaired proton to the unpaired neutron.

The $I^\pi = 8^-$ isomeric state is believed to have the single-particle structure $\pi d_{5/2} \otimes \nu h_{11/2}$. These conclusions come from the measured values for the magnetic [33] and quadrupole [32] moments and the reader is referred to these works for a full discussion.

The majority of the newly observed spherical states are those placed above the isomer. Of these, the intensely popu-

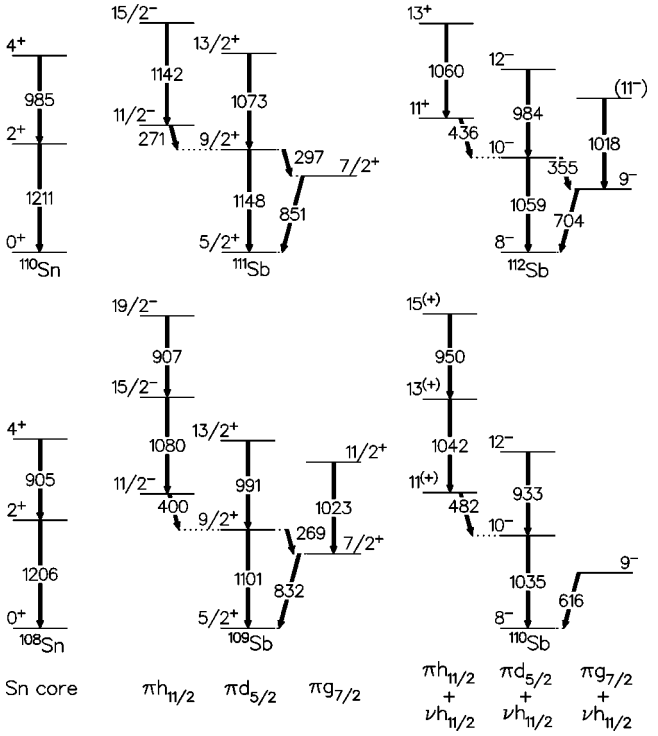

FIG. 10. Systematics of low-spin spherical states in ^{110}Sn [40,41] and ^{111}Sb [5] compared to the spherical states immediately at and above the 8^- isomer in ^{112}Sb. A similar comparison with the appropriate core nuclei [6,7] is made for ^{110}Sb [10]. The states shown in ^{109,111}Sb correspond to the weak coupling of the marked proton orbitals to the ^{108,110}Sn core nuclei. Weak coupling of the $h_{11/2}$ neutron to the states in ^{109,111}Sb results in the states shown in ^{110,112}Sb.

lated states immediately above the isomer are reproduced in Fig. 10, where they are compared to the neighboring odd-mass antimony and even-mass tin nuclei. It is apparent that there is a remarkable similarity between the states, allowing one to draw various conclusions assuming weak coupling of the odd proton and odd neutron to the ^{110}Sn [40,41] and ^{111}Sb [5] core nuclei, respectively. Reference [5] interprets the various states in ^{111}Sb in terms of the couplings of the odd proton to the 0^+, 2^+, and 4^+ states in the ^{110}Sn core. The indicated states in ^{112}Sb are those same states in ^{111}Sb weakly coupled to the $h_{11/2}$ neutron. Such an interpretation is not new, the dominant two-quasiparticle components having been discussed previously for the adjacent ^{114,116}Sb nuclei in which similar systematic structures have been observed [36,37]. Spherical states above an 8^- isomer have also been observed recently in ^{110}Sb [10], and the comparison in Fig. 10 of ^{110}Sb with its core nuclei ^{109}Sb [6] and ^{108}Sn [7] reveals similar systematic features.

There are other irregularly spaced (probably spherical) states observed in ^{112}Sb. A proper explanation of these requires extensive shell-model calculations beyond the scope of the present work. The rest of this paper concentrates on the prolate collectivity induced by proton particle-hole excitations across the $Z=50$ shell gap.

C. Band 4: $\pi g_{9/2}^{-1}\otimes\nu h_{11/2}$ configuration

A strongly coupled rotational band containing a $9^-\rightarrow 8^-$ transition with energy around 200 keV is known in all

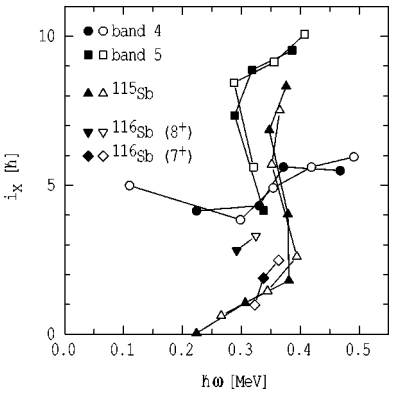

FIG. 11. Aligned angular momenta for bands 4 and 5, using the reference parameters $\Im_0=17$ MeV^{-1} $\hbar^2$ and $\Im_1=12$ MeV^{-3} $\hbar^4$, chosen previously to describe the $\pi g_{9/2}^{-1}$ bands in nearby odd-mass antimony isotopes [42]. Also shown are the alignment curves for the $\pi g_{9/2}^{-1}$ band in ^{115}Sb [43] and the $\pi g_{9/2}^{-1}\otimes\nu d_{5/2}$ (7^+) and $\pi g_{9/2}^{-1}\otimes\nu g_{7/2}$ (8^+) bands in ^{116}Sb [38].

of the odd-odd antimony isotopes from $A=108$ to $A=120$ [10,26,27,34–39]. These bands have been interpreted as being due to the $\pi g_{9/2}^{-1}\otimes\nu h_{11/2}$ configuration, where the $\pi g_{9/2}$ hole is generated by a proton 1p-1h excitation which drives the nucleus to a prolate deformation. The high-K nature of the $\pi g_{9/2}$ hole results in a strongly coupled band with intense $M1$ transitions, and since the high-K hole contributes little alignment, the aligned angular momentum for the band should show only the effects of the odd neutron. Figure 11 shows the aligned angular momenta for band 4 using the reference parameters $\Im_0=17$ MeV^{-1} $\hbar^2$ and $\Im_1=12$ MeV^{-3} $\hbar^4$, which have been used previously to describe the $\pi g_{9/2}^{-1}$ bands in the nearby ^{117,119}Sb isotopes [42]. Band 4 shows a large initial alignment of $\sim 5\hbar$, consistent only with the $h_{11/2}$ neutron. Furthermore, the first particle alignment predicted by cranked shell-model calculations is that due to $h_{11/2}$ neutrons, occurring at $\hbar\omega=0.37$ MeV (see, for example, Ref. [26]). The alignment curve for the $\pi g_{9/2}^{-1}$ band from ^{115}Sb [43] is shown in Fig. 11 and exhibits this alignment. However, this first crossing is blocked for band 4 having the $\pi g_{9/2}^{-1}\otimes\nu h_{11/2}$ configuration and is not observed.

The geometric model can be used to interpret the crossover/cascade branching ratios measured for the $\Delta I=1$, $M1/E2$ and $\Delta I=2$, $E2$ transitions in band 4. In particular, the dipole mixing ratios can be determined from the well-known relation

$$\frac{1}{\delta^2}=\frac{1}{\lambda}\left[\frac{E_\gamma(I\rightarrow I-2)}{E_\gamma(I\rightarrow I-1)}\right]^5\frac{\langle IK20|I-2K\rangle^2}{\langle IK20|I-1K\rangle^2}-1, \qquad (3)$$

where E_γ is in units of MeV and $\lambda=I_\gamma(\Delta I=2)/I_\gamma(\Delta I=1)$. Although the sign of the mixing ratio for the $M1/E2$ cascade transitions cannot be determined from Eq. (3), the measured DCO ratios for transitions in band 4 indicate they must be positive. Table VI shows the results of applying Eq. (3) to the measured branching ratios using the value $K=5$, appropriate for the $\pi g_{9/2}^{-1}\otimes\nu h_{11/2}$ configuration. The magnitudes of the mixing ratios obtained from the DCO ratios [e.g., $\delta=0.120(25)$ for the 381 keV transition] are in reasonable

TABLE VI. Properties deduced from crossover/cascade branching ratios in ^{112}Sb.

Band	I ($\hbar$)	E_γ (keV)	$\lambda = \frac{I_\gamma(\Delta I=2)}{I_\gamma(\Delta I=1)}$	δ	$B(M1)/B(E2)$ (μ_N^2/e^2 b^2)
4	10	325.5	0.035(3)	0.069(3)	24(2)
	11	353.9	0.141(7)	0.080(2)	16.0(8)
	12	380.6	0.189(9)	0.081(2)	14.2(7)
	13	392.4	0.239(13)	0.078(2)	13.3(7)
	14	406.9	0.50(3)	0.103(3)	6.8(4)
	15	486.3	0.32(3)	0.091(3)	10.6(8)
	16	503.0	0.52(5)	0.090(4)	9.9(9)
5	(12)	372.6	0.43(3)	0.109(3)	7.5(5)
	(13)	326.8	0.218(17)	0.060(2)	15.3(12)
	(14)	294.9	0.045(7)	0.026(2)	56(7)
	(15)	317.8	0.009(8)	0.013(4)	200(180)
	(16)	355.8	0.070(9)	0.036(2)	30(3)
	(17)	391.6	0.105(14)	0.040(2)	26(3)

agreement with these results. Also shown in Table VI are the $B(M1)/B(E2)$ ratios deduced using the standard expression

$$\frac{B(M1;I\rightarrow I-1)}{B(E2;I\rightarrow I-2)} = 0.6969\frac{E_\gamma^5(E2)}{E_\gamma^3(M1)}\,\frac{1}{\lambda(1+\delta^2)}\left(\frac{\mu_N}{e\ \mathrm{b}}\right)^2, \tag{4}$$

where the γ-ray energies are in units of MeV and the values of δ^2 are obtained from the solution to Eq. (3).

Figure 12(a) compares the experimental $B(M1)/B(E2)$ ratios for band 4 with calculations according to the geometrical model of Dönau [44]. Since both the strongly coupled bands observed in ^{112}Sb have no signature splitting, the following simple theoretical expressions have been applied:

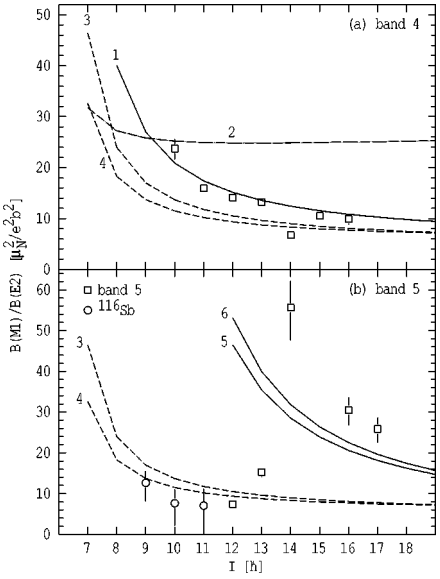

FIG. 12. $B(M1)/B(E2)$ ratios for bands 4 and 5 compared to Dönau calculations. The labels on the curves refer to the configurations given in Table VII. Also shown in the lower panel are experimental $B(M1)/B(E2)$ ratios deduced for the $\pi g_{9/2}^{-1}\otimes\nu d_{5/2}$ band in ^{116}Sb from the γ-ray intensities in Ref. [38].

$$B(M1) = \frac{3}{8\pi}\left[\sqrt{1-\frac{K^2}{I^2}}\sum_j\,[(g_K)_j - g_R]K_j - \frac{K}{I}\sum_j\,[(g_K)_j - g_R]i_j\right]^2, \tag{5}$$

$$B(E2) = \frac{15}{32\pi}\,\frac{(I-1-K)(I-1+K)(I-K)(I+K)}{(I-1)I(2I-1)(2I+1)}e^2Q_0^2, \tag{6}$$

where the sums are made over the j quasiparticles in the configuration and $(g_K)_j$, K_j, and i_j are the g factor, K projection, and aligned angular momentum, respectively, of each individual quasiparticle. Certain approximations and assumptions enter into these calculations, in particular relative to the K projections and alignments which are used for each quasiparticle. The parameters which result in each calculated curve in Fig. 12 are summarized in Table VII. Values in the table for the empirical g factors were taken from Ref. [45], while Z/A was used for the rotational g factor. The value for the quadrupole moment was taken from Ref. [34], where $Q_0 = 2.7\ e$ b was deduced for the $\pi g_{9/2}^{-1}\otimes\nu h_{11/2}$ band in ^{108}Sb from total Routhian surface calculations. This value was chosen for the purpose of comparison with the calculations of Refs. [26,34], both of which use this value. The value deduced for the $\pi g_{9/2}^{-1}$ configurations in ^{112}Sb from total Routhian surface calculations is $Q_0 = 2.9\ e$ b. Using this value would decrease the calculated curves in Fig. 12 by $\sim$15%. It will be obvious in the comparisons given below that such a change does not affect the major conclusions drawn from Fig. 12.

The current calculations confirm that the $\pi g_{9/2}^{-1}\otimes\nu h_{11/2}$ configuration (label 1) is in better agreement with experiment than the two alternative possibilities coupling either $d_{5/2}$ (label 3) or $g_{7/2}$ (label 4) neutrons to the $g_{9/2}$ proton hole. The calculations for ^{112}Sb by Singh *et al.* [26] appear to use the same parameters as the current calculation; however, there are significant differences between the two calculated curves. Furthermore, the experimental $B(M1)/B(E2)$ values

TABLE VII. Quasiparticle (qp) parameters used for the $B(M1)/B(E2)$ calculations.

Configuration[a]	Quasiparticles														
	qp	i	K	g_K	qp	i	K	g_K	qp	i	K	g_K	qp	i	K	g_K
1	$\pi g_{9/2}$	0.0	4.5	+1.27	$\nu h_{11/2}$	5.5	0.5	−0.21								
2	$\pi g_{9/2}$	0.0	4.5	−1.27[b]	$\nu h_{11/2}$	5.5	0.5	−0.21								
3	$\pi g_{9/2}$	0.0	4.5	+1.27	$\nu d_{5/2}$	2.5	0.5	−0.33								
4	$\pi g_{9/2}$	0.0	4.5	+1.27	$\nu g_{7/2}$	3.5	0.5	+0.21								
5	$\pi g_{9/2}$	0.0	4.5	+1.27	$\nu d_{5/2}$	2.5	0.5	−0.33	$\nu h_{11/2}$	5.5	0.5	−0.21	$\nu h_{11/2}$	4.5	1.5	−0.21
6	$\pi g_{9/2}$	0.0	4.5	+1.27	$\nu g_{7/2}$	3.5	0.5	+0.21	$\nu h_{11/2}$	5.5	0.5	−0.21	$\nu h_{11/2}$	4.5	1.5	−0.21

[a]Configuration labels are the same as those in Fig. 12.

[b]The g factor of the $\pi g_{9/2}$ orbital is positive. A negative value is assumed for configuration 2 for comparative purposes only (see text).

in Ref. [26] are somewhat different from the current results, in particular, having a smaller magnitude at the lower-spin values. Also, according to the information presented by Cederkäll *et al.* [34], the current $B(M1)/B(E2)$ calculations should be very similar to the results of their calculation for ^{108}Sb, since the current work uses the same set of parameters. However, the ordering in magnitude of the curves for the $\pi g_{9/2}^{-1}\otimes\nu h_{11/2}$, $\pi g_{9/2}^{-1}\otimes\nu d_{5/2}$, and $\pi g_{9/2}^{-1}\otimes\nu g_{7/2}$ configurations shown in Fig. 12(a) is the opposite of that given in Ref. [34]. To reproduce the ordering of the curves in Ref. [34], it appears to be necessary to use the incorrect sign of the g factor for the $g_{9/2}$ proton hole. The current calculation labeled 2 uses the wrong sign of this g factor for the $\pi g_{9/2}^{-1}\otimes\nu h_{11/2}$ configuration and is in reasonable agreement with the calculation of Ref. [34].

D. Band 5: $\pi g_{9/2}^{-1}\otimes\nu(d_{5/2}/g_{7/2})h_{11/2}^2$ configuration

Band 5 is not connected to the rest of the level scheme and has unknown spins and parity. The aligned angular momentum curve for band 5 shown in Fig. 11 results from using the spins marked on the level scheme in Fig. 1. Since experimental results indicate these tentative spins are most likely lower limits, the alignment curve as shown in Fig. 11 could increase in magnitude, but the slope would not change markedly, were the spins to increase. A 1p-1h proton excitation across the shell gap, leaving a high-K $\pi g_{9/2}$ hole, must be part of the band configuration, since the band is strongly coupled and the alignment above 0.3 MeV shares approximately the same slope as that for band 4, indicating a similar deformation. Recall that for band 4 it is the coupling of a rotation-aligned $h_{11/2}$ neutron to the $\pi g_{9/2}$ hole which gives an aligned angular momentum of $\sim 5\hbar$. Alternative couplings of either a $g_{7/2}$ or $d_{5/2}$ neutron to the $\pi g_{9/2}$ hole would result in a smaller aligned angular momentum than for band 4, which is clearly not the case experimentally for band 5. Thus, to explain the large aligned angular momentum requires band 5 to be built upon a four-quasiparticle excitation.

The obvious possibility to consider is the $\pi g_{9/2}$ proton hole coupled to a three-quasineutron configuration, since the presence of the $Z=50$ shell gap makes a three-quasiproton configuration unlikely. Furthermore, the large alignment points towards a $\nu h_{11/2}$ component, and since the first pair of particles to align is the $h_{11/2}$ neutron pair, energy considerations suggest that the most likely possibility for the neutron configuration is $(d_{5/2}/g_{7/2})h_{11/2}^2$. A band built on this configuration would have positive parity and approximately $(10-12)\hbar$ of aligned angular momentum, consistent with the limits on the experimental spins. If a perpendicular coupling between the (rotation-aligned) neutrons and (deformation-aligned) proton hole is assumed, a bandhead spin of $I\sim 13\hbar$ can be deduced. This corresponds to the point where the alignment curve shows a kink, which could be interpreted as the $h_{11/2}$ neutron alignment. Hence, below the alignment, band 5 would have the $\pi g_{9/2}^{-1}\otimes\nu(d_{5/2}/g_{7/2})$ configuration. The fact that the continuation of the band below the backbend is not observed is probably because the band is only near yrast above the backbend.

In fact, recent investigations of ^{116,118}Sb [38] have identified the rotational bands built upon the $\pi g_{9/2}^{-1}\otimes\nu d_{5/2}$ and $\pi g_{9/2}^{-1}\otimes\nu g_{7/2}$ configurations. These studies utilized (^{4}He,xn) reactions to populate the bands, which are nonyrast near the bandheads and are thus not populated with heavy-ion reactions [38]. This is consistent with the nonobservation of the low-spin states from band 5 in the current work. The aligned angular momenta of the $\pi g_{9/2}^{-1}\otimes\nu d_{5/2}$ and $\pi g_{9/2}^{-1}\otimes\nu g_{7/2}$ bands in ^{116}Sb are shown in Fig. 11, labeled by their bandhead spins 7^+ and 8^+, respectively. Both of these curves look like they could possibly be extensions of band 5 below the backbend, supporting the current assignment. Furthermore, the resultant (extended) alignment curves look remarkably like the $\pi g_{9/2}^{-1}$ band in ^{115}Sb, displaced slightly lower in frequency and with $\sim(1-2)\hbar$ of alignment added. This is completely consistent with band 5 in ^{112}Sb resulting from the $\pi g_{9/2}$ proton hole coupled to either the $d_{5/2}$ or $g_{7/2}$ neutron. The slight displacement in the frequency of the $\nu h_{11/2}^2$ alignment could be due to a number of factors; a likely possibility is a reduction of pairing due to blocking in the doubly odd nucleus.

Further evidence that band 5 is built upon the $\pi g_{9/2}^{-1}\otimes\nu d_{5/2}/g_{7/2}$ configuration can be obtained from a comparison of the measured $B(M1)/B(E2)$ ratios (see Table VI) with calculations from the geometrical model [see Fig. 12(b)]. Above $I=13$, corresponding to the region above the quasiparticle alignment, the measured $B(M1)/B(E2)$ ratios are reasonably close to those predicted for the $\pi g_{9/2}^{-1}\otimes\nu(d_{5/2}/g_{7/2})h_{11/2}^2$ configurations (labels 5 and 6). Below $I=13$, the ratios are close to those calculated for the $\pi g_{9/2}^{-1}\otimes\nu(d_{5/2}/g_{7/2})$ configurations (labels 3 and 4), as would be expected below the $\nu h_{11/2}^2$ alignment. The intensities from

Ref. [38] have been used to deduce the experimental $B(M1)/B(E2)$ ratios for the $\pi g_{9/2}^{-1} \otimes \nu d_{5/2}$ band in ^{116}Sb. These points are also plotted in Fig. 12(b) and show reasonable agreement with both the calculated values (label 3) and an extrapolation of the measured $B(M1)/B(E2)$ ratios for band 5 to lower spin. (The agreement of the extrapolation rests upon the likely assumption that the bands in ^{112}Sb and ^{116}Sb have similar deformations.)

The $\pi g_{9/2}^{-1} \otimes \nu (d_{5/2}/g_{7/2}) h_{11/2}^2$ configuration possesses characteristics that could explain the fragmented decay of band 5. It would have positive parity, and so the partial decay to positive-parity levels at the bottom right of the level scheme in Fig. 1 may be expected. The decay towards negative-parity states in band 4 can also be explained because the configuration for band 5 differs from that for band 4 by a $\nu[(d_{5/2}/g_{7/2}) - h_{11/2}]$ excitation. The interaction between the $d_{5/2}$ and $h_{11/2}$ orbitals is related to the onset of octupole deformation and the occurrence of parity-changing transitions [46]. Also, two bands with similar behavior to bands 4 and 5 in ^{112}Sb have been observed recently in ^{110}Sb [10,47]. In the ^{110}Sb nucleus, the (assumed) $E1$ transitions linking the two bands have been observed. The band in ^{110}Sb which would be equivalent to band 5 in ^{112}Sb also shows a partial (unobserved) decay towards positive-parity states near the ground state and a decay component feeding the 8^- isomer.

E. Decoupled bands and smooth band termination

Recent studies of rotational bands built upon 2p-2h proton excitations in the $A \approx 110$ region have revealed that at the very highest spins the bands gradually lose their collectivity and eventually terminate at a spin corresponding to the sum of the spins of the individual valence nucleons. This is because, with the small number of valence particles outside the Z and $N = 50$ closed shells, the total angular momentum for configurations with one to three holes in the $\pi g_{9/2}$ subshell is limited to $\sim (30-50)\hbar$. As the nucleus rotates, the valence particles gradually align their spins to the rotation axis and the nuclear shape is predicted [13,14] to change over many transitions from collective near prolate ($\gamma \approx 0°$) at low spin to noncollective oblate ($\gamma = +60°$) at the band termination. The changing shape and consequent reduction in collectivity was confirmed by lifetime measurements for the first time recently [15], for two bands in ^{108}Sn and one band in ^{109}Sb, providing important proof that a smooth termination process is taking place. Smooth terminating bands are now known to near termination spins in a number of nuclei in the $A \approx 110$ region, including ^{106,108,109}Sn [7–9], ^{109,110,111,113}Sb [5,6,10,48], and ^{114,116}Te [11,49]. The reason for the profusion of terminating bands in this region is because of (i) the limited valence space outside of the double-shell closure at ^{100}Sn and (ii) specific configurations found to be yrast over a large spin range and thus observed from low spin up to termination.

The main experimental characteristic of the terminating bands in the $A \approx 110$ region is a decrease of the dynamic moment of inertia ($\mathcal{J}^{(2)} \approx 4/\Delta E_\gamma$) with spin to unusually low values, a fraction of the rigid-body value. The increase in the γ-ray energy spacings which is apparent in Fig. 8 for bands 2 and 3, and especially band 1, in ^{112}Sb, implies such a decreasing dynamic moment of inertia (see Fig. 13). These low values of $\mathcal{J}^{(2)}$ correspond to the fact that the building of the last spin units before termination has a large energy cost, determined mainly from (i) the difficulty of aligning the high-K, $\pi g_{9/2}$ holes and (ii) the fact that the neutron $(d_{5/2}/g_{7/2})$ subshells are essentially half-filled [14]. This unfavored band termination manifests as a characteristic minimum when the excitation energy is plotted versus spin in the form $E - E_{\mathrm{RLD}}$, where E_{RLD} is a rigid-rotor reference. The position and shape of the minima, together with the terminating spin of a band, are configuration dependent and provide easy points of identification when making comparisons with theoretical calculations. Such plots for ^{112}Sb are discussed further below.

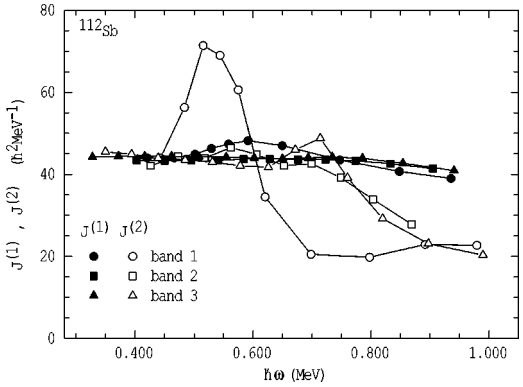

FIG. 13. Static and dynamic moments of inertia for the three decoupled bands observed in ^{112}Sb.

There is a well-developed theoretical understanding [13,14,50] of smooth band termination in terms of calculations using the configuration-dependent cranked Nilsson-Strutinsky model, with techniques that allow the identification of specific single-particle configurations to high spin. Such calculations have been performed for ^{112}Sb for the present work and the results are presented in Fig. 14 in the form of excitation energies with a rigid-rotor reference subtracted, for the four combinations of parity and signature. Pairing correlations have been neglected in the calculations and the parameter set from Ref. [51] has been used for the Nilsson potential. Three particular rotational bands are predicted to lie lowest in energy over the spin range $(25-40)\hbar$. These are the favored signature of the [21,3] and the two signatures of the [21,4] configuration. (The notation used here to describe the configurations is the same as in Ref. [14], namely, $[p_1 p_2, n]$ where p_1 is the number of $g_{9/2}$ proton holes, p_2 the number of $h_{11/2}$ protons, n the number of $h_{11/2}$ neutrons, and with the remaining valence particles outside of ^{100}Sn distributed across the positive-parity $d_{5/2}/g_{7/2}$ subshells.) The presence of these configurations near the yrast line is not surprising considering that in the neighboring isotope ^{111}Sb the three bands which are known are the two signatures of the [21,3] and the favored signature of the [21,4] configuration [5,14], while in ^{113}Sb, the favored signature of the [21,4] configuration is known [52]. The intervening ^{112}Sb nucleus might be expected to exhibit these same two configurations.

The experimental energies of the three decoupled bands in ^{112}Sb are plotted in Fig. 15 with a rigid-rotor reference subtracted. For the unlinked band 3, the approximate excitation

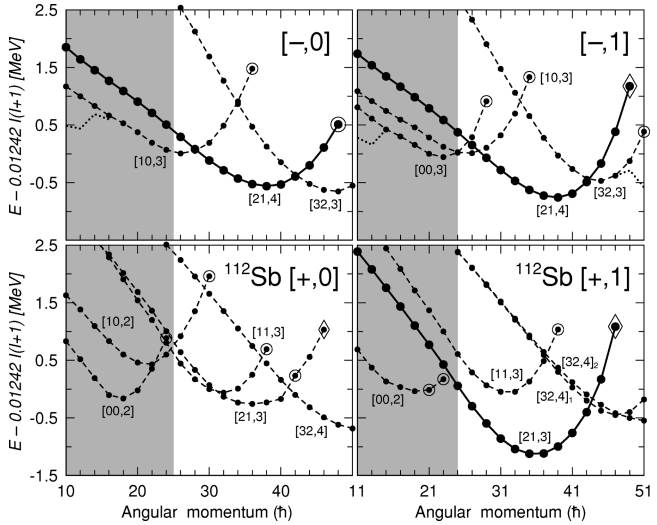

FIG. 14. Calculated yrast configurations of ^{112}Sb, shown with a rigid-rotor reference subtracted, for the four combinations of parity π and signature α. The shorthand configuration labeling is explained in the text. The subscripts used with this notation are for the cases where the same [32,4] configuration with $[+,1]$ parity and signature is obtained as a consequence of the different distributions of proton holes in the $g_{9/2}$ and neutrons in the $g_{7/2}d_{5/2}$ orbitals. Large open circles are used to indicate terminating states. Large open diamonds are used in the cases where the terminating states involve contributions from the $\nu d_{3/2}s_{1/2}$ orbitals. Solid lines are used for configurations assigned to observed bands (see Fig. 15), while other (unobserved) configurations are shown by dashed lines. A shaded background indicates the spin range where pairing correlations could be of some importance.

energy has been deduced using the assumption that band 3 is the signature partner to band 2 and is thus energy degenerate with band 2 at the lowest observed spins. These experimental curves can be compared to the three bands calculated to lie

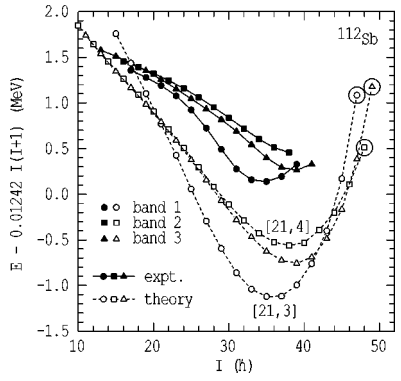

FIG. 15. Experimental energies of states in the decoupled bands in ^{112}Sb with a rigid-rotor reference subtracted. The results of theoretical calculations for the three rotational bands calculated to lie lowest in energy are plotted in the same way for comparison. Because of the neglect of pairing in the calculations, only the shapes of the curves and the relative energies of the experimental bands should be compared with the predictions of theory. The theoretical curves are labeled by their configurations, with the predicted terminating states marked by large open circles. Note that band 3 does not have well-defined spin, parity, or excitation energy (see Figs. 1 and 9 and the text).

lowest in ^{112}Sb; the curves for the lowest three theoretical bands have been extracted from Fig. 14 and are reproduced in Fig. 15. When comparing theory and experiment, it must be remembered that pairing correlations are neglected in the calculations. As a result, the comparison should not be carried out with respect to the low-spin states, but with respect to one of the high-spin states. Experience with these theoretical comparisons suggests that with decreasing spin below $25\hbar$, larger discrepancies can be expected due to the increasing role of pairing correlations.

In making the comparison between theory and experiment in Fig. 15, a natural interpretation presents itself; that is, band 1 is the favored signature of the [21,3] configuration, while bands 2 and 3 are the two signatures of the [21,4] configuration. There is excellent agreement for all aspects of the calculations, including that (i) the predicted configurations agree with the experimental signatures and parities, (ii) the details of the $E-E_{\mathrm{RLD}}$ curves with respect to the spin positions of the energy minima are reproduced, and (iii) the ordering of the different bands in excitation energy is consistent with experiment. With respect to point (iii), it is noteworthy that there is also rather good agreement obtained for the differences in excitation energies between the bands. Although band 3 is not linked to the low-spin-level scheme, the agreement with theory gives some confidence that the correct spins and approximate excitation energy have been deduced for the band.

None of the bands are observed up to their terminations, with typically four more transitions expected to reach the terminating states. Note that this means for all the bands, termination would require eight more units of spin at a point on the $E-E_{\mathrm{RLD}}$ curve where the extra units of spin are energetically expensive to generate. Note also that the maximum spins to which the bands are observed are approximately those where the bands are predicted to be crossed by bands built upon 3p-3h proton excitations (see Fig. 14). The nonobservation of the bands to higher spins could be because the channel intensity instead feeds into the bands built upon 3p-3h configurations. On the other hand, it could simply be due to limitations in the resolving power of the current experiment. In any case, the observation of the terminating states of smooth terminating bands in nuclei with masses around $A\approx 112$ and above is difficult because the terminating states have spins approaching $50\hbar$. An experiment performed on a large detector array with an optimal reaction to populate ^{112}Sb could possibly observe the terminating states. However, perhaps even more important than the observation of the terminating states of the 2p-2h configurations would be the observation of the bands built upon 3p-3h proton configurations. This also could possibly be addressed by a more powerful experiment.

The isotopes lighter than ^{112}Sb generally show a very good detailed agreement between the theoretical and experimental shapes of the $E-E_{\mathrm{RLD}}$ curve near the minima and up to termination (see, for example, Fig. 4 of Ref. [10] for ^{110}Sb). This contrasts with the heavier isotopes for which there is an experimental trend towards a flatter $E-E_{\mathrm{RLD}}$ curve which is not as well reproduced by theory (see, for example, Fig. 5 of Ref. [52] for ^{113}Sb and Fig. 3 of Ref. [11] for ^{114}Te). The results for ^{112}Sb agree with this trend, lying somewhere between these two extremes. A possible explana-

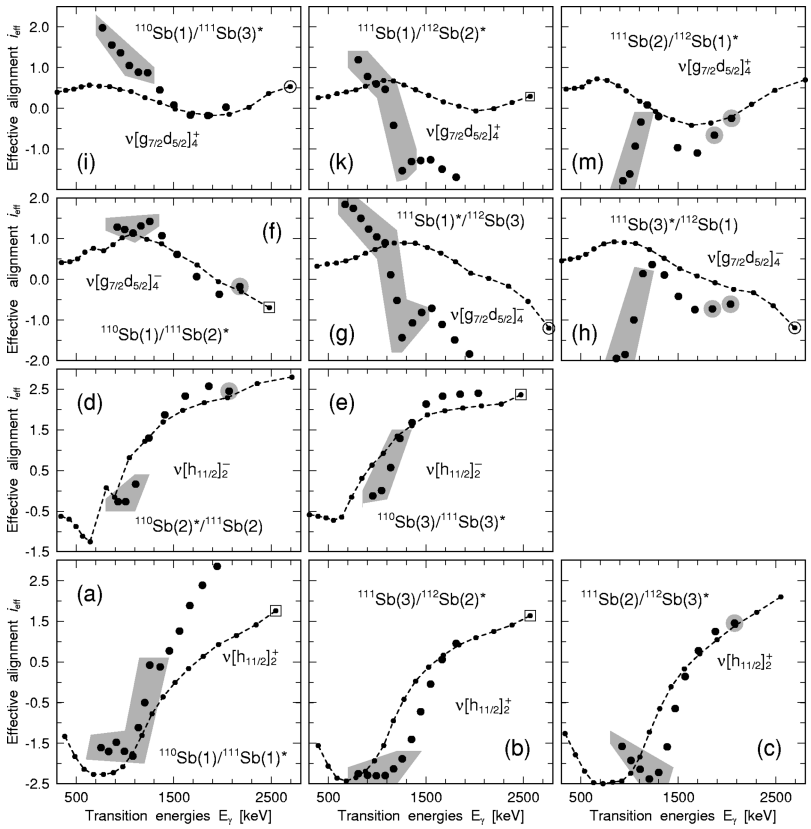

FIG. 16. Effective alignments $i_{\rm eff}$ (in units of $\hbar$) associated with the occupation of different neutron orbitals, extracted from the experimental bands (unconnected large symbols). The results are compared with those extracted from the calculated configurations assigned to the bands (connected small symbols). The experimental effective alignment between bands A and B is indicated as ''A/B.'' Band A in the lighter nucleus is taken as a reference; hence, the effective alignment measures the effect of the additional particle. The compared configurations differ by the occupation of the orbitals indicated on the panels. These orbitals are labeled by (i) the dominant components of their wave functions at zero rotational frequency, (ii) the sign of their signature α given as a superscript, and (iii) the position of the orbitals within the specific signature group given as a subscript (see, for example, Fig. 3 of Ref. [50]). Note also that the $i_{\rm eff}$ values are shown at the transition energies of the shorter band marked with an asterisk (*). The points corresponding to transitions depopulating terminating states are encircled. When $I_{\rm max}$ has not been reached, the points corresponding to transitions depopulating the states with spin $(I_{\rm max}-2)$ are indicated by large open squares. These symbols are not used when the configurations of the bands, marked by an asterisk, involve the $(d_{3/2}s_{1/2})$ orbital close to termination. The experimental points which appear to be affected either by pairing interactions or by unpaired band crossings (as follows, for example, from the analysis of the $\mathcal{J}^{(2)}$ of the bands) are shown on a shaded background.

tion is that for the heavier isotopes with more available valence nucleons the level density is higher and the absence of pairing becomes a more extreme approximation, especially for the more nonyrast states away from the $E-E_{\rm RLD}$ minimum.

F. Relative properties of smooth terminating bands observed in the chain $^{110-112}$Sb

As discussed in Ref. [50] in detail, the relative properties of the observed bands can be studied by means of an effective alignment approach. This approach provides an additional and very sensitive tool for the interpretation of observed bands, especially in the cases when they are not linked to the low-spin-level scheme. The effective alignment of two bands A and B is simply the difference between their spins at constant γ-transition energy E_γ (or, equivalently, rotational frequency $\hbar\omega$) [53]:

$$i_{\rm eff}^{B,A}(E_\gamma)=I^B(E_\gamma)-I^A(E_\gamma). \qquad (7)$$

Experimentally, $i_{\rm eff}$ measures the contribution(s) from the orbital(s) which are occupied in band B and empty in band A. These contributions include both the alignment(s) of the single-particle orbital(s) and the effects associated with changes in deformation, pairing, etc., between the two bands. This approach exploits the fact that spin is quantized, integer for even nuclei and half-integer for odd nuclei, and, furthermore, constrained by signature. With the configurations and specifically the signatures fixed, the relative spins of the observed bands can only change in steps of $\pm 2\hbar n$ (n is an integer number).

The effective alignment approach has been used with reasonable success in Ref. [50] for the study of relative properties of smooth terminating bands observed in ^{108,109}Sn [7,8] and ^{109,110}Sb [6,10]. A similar investigation is presented here for the smooth terminating bands observed in the chain $^{110-112}$Sb [5,10], the results of which are shown in Fig. 16. All smooth terminating bands observed in these nuclei have been used in the analysis. Among these bands, only band 1 in

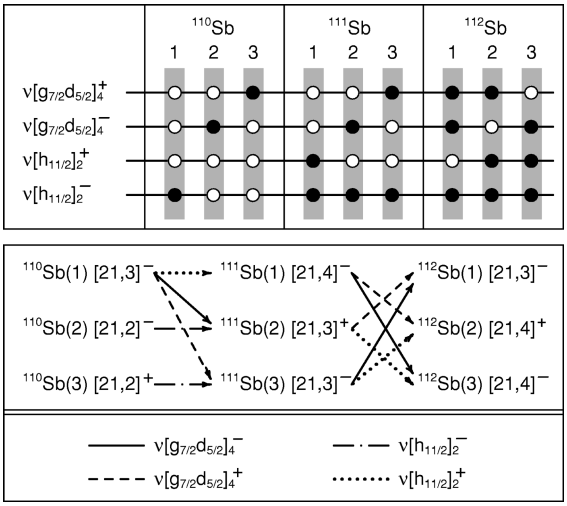

FIG. 17. Smooth terminating bands observed in ^{110,111,112}Sb [5,10] (middle panel). The assigned configurations are indicated after the band labels. The total signature of a configuration, $\alpha_{\rm tot}$, is shown as a superscript as described in the text. The differences in the configurations of the observed bands are indicated by arrows of different types which relate to specific orbitals. The correspondence between the type of arrow and the orbital is given in the bottom panel. Note that only the pairs of bands which differ by occupation of one orbital are compared. The occupation of different neutron orbitals in the configurations assigned to bands observed in $^{110-112}$Sb (top panel). Note that the $[g_{7/2}d_{5/2}]_{1,2,3}$ orbitals as well as the $[h_{11/2}]_1$ orbitals are occupied in all bands and thus are not shown. Proton configurations of all the bands are the same with two proton holes in $g_{9/2}$, two protons in $(g_{7/2}d_{5/2})$, and one proton in $h_{11/2}$ with signature $\alpha=-1/2$.

^{110}Sb, band 1 in ^{111}Sb, and bands 1 and 2 in ^{112}Sb are linked to the low-spin-level scheme. The configurations and spin-parity assignments given in the original articles have been used, including those suggested for the unlinked bands [10,14]. All pairs of bands, which, according to the present assignments, differ by a particle in one orbital, have been included in the comparison. Details of the bands which are discussed, their configuration assignments and the single-particle differences between them, are summarized in Fig. 17. Note that in Fig. 17 the total signature of the configuration is denoted by a superscript ($+$ or $-$). Since the signature depends on the type of nucleus (even or odd), the following simplified notation is used: $(\alpha_{\rm tot}=+)\equiv[\alpha_{\rm tot}=+1/2\ ({\rm odd})]\equiv[\alpha_{\rm tot}=0\ ({\rm even})]$, $(\alpha_{\rm tot}=-)\equiv[\alpha_{\rm tot}=-1/2\ ({\rm odd})]\equiv[\alpha_{\rm tot}=+1({\rm even})]$.

The comparisons of the relative properties of the bands, which are presented in Fig. 16, are generally successful in interpreting the band structures; however, there is disagreement for a specific band, which could be an experimental problem. This specific disagreement between experiment and theory occurs for the pairs involving band 1 in ^{111}Sb; see Figs. 16(a), 16(g), and 16(k). In addition, the calculated $E-E_{\rm RLD}$ plot for this band deviates significantly from that for the assigned $[21,4]^-$ configuration (see Ref. [14]). Also, the properties of this band deviate significantly from the experimental systematics of the 2p-2h bands observed in the $^{109-112}$Sb chain [54]. The slopes of the calculated and experimental alignments in the ^{111}Sb(1)/^{112}Sb(2) and ^{111}Sb(1)/^{112}Sb(3) pairs [see Figs. 16(g) and 16(k)] are very similar at $E_\gamma\geqslant 1500$ keV, where the pairing correlations are of small importance, but the difference in absolute value between theory and experiment is approximately $2\hbar$. This is accompanied by a similar difference with opposite sign when the ^{111}Sb(1) band is compared with the ^{110}Sb(1) band [see Fig. 16(a)]. Consequently, if the ^{112}Sb(2,3) bands were compared with the ^{110}Sb(1) band, a reasonably good agreement would be obtained. This shows that it is really band 1 in ^{111}Sb which causes the problems. Note that the lowering of the assigned spin values by $2\hbar$ for band 1 in ^{111}Sb will bring the experimental alignments closer to those calculated at the highest observed frequencies. In addition, such a change will result in better agreement between the calculated and experimental $E-E_{\rm RLD}$ plots at spins $I\geqslant 30\hbar$. Because of these uncertainties, the pairs involving this band will not be discussed below.

At low rotational frequencies of $\hbar\omega\leqslant 0.6-0.7$ MeV, the observed bands can be affected by pairing correlations as follows from the features of their dynamic moments of inertia. Cranked Woods-Saxon calculations performed for ^{111}Sb in Ref. [5] predict an $h_{11/2}$ neutron crossing to occur at $\hbar\omega=0.35$ MeV and a $g_{7/2}$ proton crossing at $\hbar\omega=0.6$ MeV. No other paired band crossings are expected theoretically in the frequency range $\hbar\omega<0.6$ MeV. The $h_{11/2}$ neutron band crossing is not seen in the effective alignments of Fig. 16 since the overlap of the compared bands does not go to such low frequencies. The proton configuration of all compared bands is the same, and so only minor effects are expected in the effective alignments due to small changes in the proton pairing field, the equilibrium deformations, etc.

The experimental effective alignments of the $[h_{11/2}]^{\pm}_2$ orbitals are reproduced in the calculations reasonably well [see Figs. 16(b), 16(c), 16(d), and 16(e)]. It is interesting to note that the $[h_{11/2}]^{+}_2$ orbital, especially, is antialigned at low rotational frequencies. This feature is most clearly seen in the ^{111}Sb(3)/^{112}Sb(2) and ^{111}Sb(2)/^{112}Sb(3) pairs [see Figs. 16(b) and 16(c)], and, in general, it is reproduced in calculations. However, the change in slope of $i_{\rm eff}$ takes place at a lower frequency in the calculations as compared with experiment. In the bands with three or four occupied $h_{11/2}$ neutrons, the increase in $\mathcal{J}^{(2)}$ observed at low frequencies (see, for example, Fig. 13) may originate not only from paired band crossings, but also from the alignment features of the third and fourth $h_{11/2}$ orbitals, which are antialigned at low frequencies (see also Fig. 3 in Ref. [50]). The antialignment of low-lying high-j orbitals has been previously found and observed over a considerable spin range in superdeformed bands (see, for example, Refs. [55,56]); however, to our knowledge, the data in Figs. 16(b) and 16(c) are the first clear evidence for similar features at normal deformation.

The alignments of the $\nu[g_{7/2}d_{5/2}]^{\pm}_4$ orbitals in the ^{110}Sb(1)/^{111}Sb(3) and ^{110}Sb(1)/^{111}Sb(2) pairs are reproduced reasonably well at transition energies larger than $\sim$1300 keV where the role of pairing correlations is of minor importance [see Figs. 16(f) and 16(i)]. In contrast, for the ^{111}Sb(2)/^{112}Sb(1) and ^{111}Sb(3)/^{112}Sb(1) pairs [Figs. 16(h) and 16(m)], although the general trends of the alignment of these orbitals are reproduced in the calculations, the discrepancies are larger. One possible explanation may be that for

heavier nuclei the level density is higher and the absence of pairing in the calculations becomes a more severe approximation.

Among the bands under study, the ^{110}Sb(2), ^{111}Sb(2), and ^{112}Sb(1) bands all show an increase in $\mathcal{J}^{(2)}$ at the highest observed rotational frequencies [see, for example, Fig. 13 for ^{112}Sb(1)]. This increase correlates with disturbances in the behavior of the experimental effective alignments at the highest observed rotational frequencies for the pairs in which one of these bands is involved [see Figs. 16(d), 16(f), 16(h), and 16(m)]. As follows from Ref. [50] and the present study, such an increase in $\mathcal{J}^{(2)}$ appears only in the bands in which the $\nu[g_{7/2}d_{5/2}]_4^-$ orbital is occupied. Only the ^{112}Sb(2) band, in which, according to the present interpretation, this orbital is occupied, does not show such an increase in $\mathcal{J}^{(2)}$ at the highest observed rotational frequencies. (Note, however, that this band is observed to the lowest rotational frequency of the three bands in ^{112}Sb.) As discussed in Ref. [50], the most probable reason for this increase in $\mathcal{J}^{(2)}$ is connected with the unpaired ''band crossing'' between the $[g_{7/2}d_{5/2}]_4^-$ orbital and the $[d_{3/2}s_{1/2}]_1^-$ orbital. It should be noted that the $[21,3]^-$ and $[21,4]^-$ configurations assigned to bands 1 and 3, respectively, terminate in the calculations at a spin $2\hbar$ higher than the ''maximum'' spin defined from the distribution of the valence particles and holes over the j shells at low spin. At ''maximum'' spin ($45\hbar$ for $[21,3]^-$ and $47\hbar$ for $[21,4]^-$), the potential energy surfaces are flat in the γ direction with a minimum at a modest collectivity lying lower by 20–40 keV than the lowest energy at the noncollective axis. As discussed in Ref. [50], this indicates the involvement of the $[d_{3/2}s_{1/2}]_1^-$ orbital close to termination. In the calculations, however, the crossing between these orbitals takes place at higher spin than is suggested from experiment. With no specific fit of the relative energies of the $(g_{7/2}d_{5/2})$ and $(d_{3/2}s_{1/2})$ subshells in the Nilsson potential, it can hardly be expected that such fine features can be reproduced in the calculations.

VI. CONCLUSIONS

New results have been presented on excited states in ^{112}Sb, including the observation of many new excited states which feed solely towards the $I^\pi = 8^-$ isomer. Five rotational bands involving particle-hole excitations across the $Z=50$ shell gap have been observed to coexist with the expected single-particle structures. Two of these are built upon 1p-1h proton excitations, one being the low-lying two quasiparticle $\pi g_{9/2}^{-1} \otimes \nu h_{11/2}$ excitation common to all the odd-odd antimony isotopes and the other being an unlinked band which has the four-quasiparticle configuration $\pi g_{9/2}^{-1} \otimes \nu(d_{5/2}/g_{7/2}) h_{11/2}^2$. [The latter band is actually due to the $\pi g_{9/2}^{-1} \otimes \nu(d_{5/2}/g_{7/2})$ configuration, but is only observed above the $\nu h_{11/2}^2$ alignment.] The configuration assignments for the 1p-1h bands are confirmed by comparison with geometric model calculations of the $B(M1)/B(E2)$ ratios. Good agreement is obtained with the geometric model calculations without the need to invoke a shears-type excitation; however, tilted-axis cranking calculations and the measurement of the absolute $M1$ transition strengths would be useful in confirming whether or not the shears mechanism is important in these bands.

Three bands built upon 2p-2h proton excitations have also been observed, and all three show the characteristics of smooth band termination. Excellent agreement with cranked Nilsson-Strutinsky calculations has been obtained for this well-determined system in which two of the smooth terminating bands have been assigned definite spins and parities from the experimental results, while the spin and parity of the third can also be reasonably deduced with some confidence. Because it is a well-understood system experimentally, the new results for ^{112}Sb provide important confirmation of the smooth band termination interpretation.

A detailed experimental and theoretical study of the relative properties of the smooth terminating bands in the chain $^{110-112}$Sb has also been performed. This confirms the configuration assignments for all of the known bands in these nuclei, except for band 1 in ^{111}Sb, which appears to cause some problems. The analysis also shows what is, to our knowledge, the first clear evidence for the antialignment of high-j orbitals at normal deformation, in this case $h_{11/2}$ neutrons.

ACKNOWLEDGMENTS

The authors would like to thank A. Lipski for fabrication of the targets and the personnel at Strasbourg and Stony Brook for their support of the experimental measurements. The first author is grateful to the staff at the Department of Nuclear Physics at the Australian National University for providing the facilities to complete both the final analysis and the writing of this paper, and for numerous helpful comments. This project has been funded in part by the U.S. National Research Council under the Collaboration in Basic Science and Engineering Program. Additional support was provided by the U.S. National Science Foundation, U.K. Engineering and Physical Sciences Research Council, and the Swedish Natural Science Research Council. A.V.A. and I.R. are grateful for financial support from the Crafoord Foundation (Lund, Sweden) and the Royal Swedish Academy of Sciences.

[1] K. Heyde, P. Van Isacker, M. Waroquier, J. L. Wood, and R. A. Meyer, Phys. Rep. **102**, 291 (1983).

[2] J. L. Wood, K. Heyde, W. Nazarewicz, M. Huyse, and P. Van Duppen, Phys. Rep. **215**, 101 (1992).

[3] A. K. Gaigalas, R. E. Shroy, G. Schatz, and D. B. Fossan, Phys. Rev. Lett. **35**, 555 (1975); R. E. Shroy, A. K. Gaigalas, G. Schatz, and D. B. Fossan, Phys. Rev. C **19**, 1324 (1979).

[4] J. Bron, W. H. A. Hesselink, A. Van Poelgeest, J. J. A. Zalmstra, M. J. Uitzinger, H. Verheul, K. Heyde, M. Waroquier, H. Vincx, and P. Van Isacker, Nucl. Phys. **A318**, 335 (1979).

[5] D. R. LaFosse, D. B. Fossan, J. R. Hughes, Y. Liang, H. Schnare, P. Vaska, M. P. Waring, J.-Y. Zhang, R. M. Clark, R. Wadsworth, S. A. Forbes, E. S. Paul, V. P. Janzen, A. Galindo-Uribarri, D. C. Radford, D. Ward, S. M. Mullins, D. Prévost, and G. Zwartz, Phys. Rev. C **50**, 1819 (1994).

[6] V. P. Janzen, D. R. LaFosse, H. Schnare, D. B. Fossan, A. Galindo-Uribarri, J. R. Hughes, S. M. Mullins, E. S. Paul, L. Persson, S. Pilotte, D. C. Radford, I. Ragnarsson, P. Vaska, J. C. Waddington, R. Wadsworth, D. Ward, J. Wilson, and R. Wyss, Phys. Rev. Lett. **72**, 1160 (1994); H. Schnare, D. R. LaFosse, D. B. Fossan, J. R. Hughes, P. Vaska, K. Hauschild, I. M. Hibbert, R. Wadsworth, V. P. Janzen, D. C. Radford, S. M. Mullins, C. W. Beausang, E. S. Paul, J. DeGraaf, I.-Y. Lee, A. O. Macchiavelli, A. V. Afanasjev, and I. Ragnarsson, Phys. Rev. C **54**, 1598 (1996).

[7] R. Wadsworth, C. W. Beausang, M. Cromaz, J. DeGraaf, T. E. Drake, D. B. Fossan, S. Flibotte, A. Galindo-Uribarri, K. Hauschild, I. M. Hibbert, G. Hackman, J. R. Hughes, V. P. Janzen, D. R. LaFosse, S. M. Mullins, E. S. Paul, D. C. Radford, H. Schnare, P. Vaska, D. Ward, J. N. Wilson, and I. Ragnarsson, Phys. Rev. C **53**, 2763 (1996).

[8] L. Käubler, H. Schnare, D. B. Fossan, A. V. Afanasjev, W. Andrejtscheff, R. G. Allat, J. DeGraaf, H. Grawe, I. M. Hibbert, I.-Y. Lee, A. O. Macchiavelli, N. O'Brien, K.-H. Maier, E. S. Paul, H. Prade, I. Ragnarsson, J. Reif, R. Schubart, R. Schwengner, I. Thorslund, P. Vaska, R. Wadsworth, and G. Winter, Z. Phys. A **356**, 235 (1996).

[9] R. Wadsworth, H. R. Andrews, C. W. Beausang, R. M. Clark, J. DeGraaf, D. B. Fossan, A. Galindo-Uribarri, I. M. Hibbert, K. Hauschild, J. R. Hughes, V. P. Janzen, D. R. LaFosse, S. M. Mullins, E. S. Paul, L. Persson, S. Pilotte, D. C. Radford, H. Schnare, P. Vaska, D. Ward, J. N. Wilson, and I. Ragnarsson, Phys. Rev. C **50**, 483 (1994).

[10] G. J. Lane, D. B. Fossan, I. Thorslund, P. Vaska, R. G. Allat, E. S. Paul, L. Käubler, H. Schnare, I. M. Hibbert, N. O'Brien, R. Wadsworth, W. Andrejtscheff, J. de Graaf, J. Simpson, I. Y. Lee, A. O. Macchiavelli, D. J. Blumenthal, C. N. Davids, C. J. Lister, D. Seweryniak, A. V. Afanasjev, and I. Ragnarsson, Phys. Rev. C **55**, R2127 (1997).

[11] I. Thorslund, D. B. Fossan, D. R. LaFosse, H. Schnare, K. Hauschild, I. M. Hibbert, S. M. Mullins, E. S. Paul, I. Ragnarsson, J. M. Sears, P. Vaska, and R. Wadsworth, Phys. Rev. C **52**, R2839 (1995).

[12] T. Bengtsson and I. Ragnarsson, Phys. Scr. **T5**, 165 (1983).

[13] I. Ragnarsson, V. P. Janzen, D. B. Fossan, N. C. Schmeing, and R. Wadsworth, Phys. Rev. Lett. **74**, 3935 (1995).

[14] A. V. Afanasjev and I. Ragnarsson, Nucl. Phys. **A591**, 387 (1995).

[15] R. Wadsworth, R. M. Clark, J. Cameron, D. B. Fossan, I. M. Hibbert, V. P. Janzen, R. Krücken, G. J. Lane, I.-Y. Lee, A. O. Macchiavelli, C. M. Parry, J. M. Sears, J. F. Smith, A. V. Afanasjev, and I. Ragnarsson, Phys. Rev. Lett. **80**, 1174 (1998).

[16] C. E. Svensson, C. Baktash, G. C. Ball, J. A. Cameron, M. Devlin, J. Eberth, S. Flibotte, A. Galindo-Uribarri, D. S. Haslip, V. P. Janzen, D. R. LaFosse, I. Y. Lee, A. O. Macchiavelli, R. W. MacLeod, J. M. Nieminen, S. D. Paul, D. C. Radford, L. L. Riedinger, D. Rudolph, D. G. Sarantites, H. G. Thomas, J. C. Waddington, D. Ward, W. Weintraub, J. N. Wilson, A. V. Afansjev, and I. Ragnarsson, Phys. Rev. Lett. **80**, 2558 (1998).

[17] R. M. Clark, R. Wadsworth, H. R. Andrews, C. W. Beausang, M. Bergstrom, S. Clarke, E. Dragulescu, T. Drake, P. J. Dagnall, A. Galindo-Uribarri, G. Hackman, K. Hauschild, I. M. Hibbert, V. P. Janzen, P. M. Jones, R. W. MacLeod, S. M. Mullins, E. S. Paul, D. C. Radford, A. Semple, J.F. Sharpey-Schafer, J. Simpson, D. Ward, and G. Zwartz, Phys. Rev. C **50**, 84 (1994).

[18] G. Baldsiefen, M. A. Stoyer, J. A. Cizewski, D. P. McNabb, W. Younes, J. A. Becker, L. A. Bernstein, M. J. Brinkman, L. P. Farris, E. A. Henry, J. R. Hughes, A. Kuhnert, T. F. Wang, B. Cederwall, R. M. Clark, M. A. Deleplanque, R. M. Diamond, P. Fallon, I.-Y. Lee, A. O. Macchiavelli, J. Oliveira, F. S. Stephens, J. Burde, D. T. Vo, and S. Frauendorf, Phys. Rev. C **54**, 1106 (1996).

[19] R. M. Clark, S. J. Asztalos, G. Baldsiefen, J. A. Becker, L. Bernstein, M. A. Deleplanque, R. M. Diamond, P. Fallon, I. M. Hibbert, H. Hübel, R. Krücken, I.-Y. Lee, A. O. Macchiavelli, R. W. MacLeod, G. Schmid, F. S. Stephens, K. Vetter, R. Wadsworth, and S. Frauendorf, Phys. Rev. Lett. **78**, 1868 (1997).

[20] S. Frauendorf, in *Proceedings of the Workshop on Gammasphere Physics*, Berkeley, 1995, edited by M. A. Deleplanque, I. Y. Lee, and A. O. Macchiavelli (World Scientific, Singapore, 1996), p. 272.

[21] S. Frauendorf, Nucl. Phys. **A557**, 159c (1993).

[22] G. J. Lane *et al.* (unpublished).

[23] R. Kamermans, H. W. Jongsma, T. J. Ketel, R. Van Der Wey, and H. Verheul, Nucl. Phys. **A266**, 346 (1976).

[24] M. Fayez-Hassan, J. Gulyás, Zs. Dombrádi, I. Dankó, and Z. Gácsi, Phys. Rev. C **55**, 2244 (1997).

[25] M. E. J. Wigmans, R. J. Heynis, P. M. A. van der Kam, and H. Verheual, Phys. Rev. C **14**, 243 (1976).

[26] A. K. Singh, G. Gangopadhyay, D. Banerjee, R. Bhattacharya, R. K. Bhowmik, S. Murilithar, G. Rodrigues, R. P. Singh, A. Goswami, S. Chattopadhyay, S. Bhattacharya, B. Dasmahapatra, and S. Sen, Nucl. Phys. **A607**, 350 (1996).

[27] C.-B. Moon, J. U. Kwon, T. Komatsubara, T. Saitoh, N. Hashimoto, J. Lu, H. Kimura, T. Haykawa, and K. Furuno, Z. Phys. A **357**, 5 (1997).

[28] E. S. Paul, D. B. Fossan, K. Hauschild, I. M. Hibbert, H. Schnare, J. M. Sears, I. Thorslund, R. Wadsworth, A. N. Wilson, and J. N. Wilson, Phys. Rev. C **51**, R2857 (1995).

[29] P. M. Jones, L. Wei, F. A. Beck, P. A. Butler, T. Byrski, G. Duchne, G. de France, F. Hannachi, G. D. Jones, and B. Kharraja, Nucl. Instrum. Methods Phys. Res. A **362**, 556 (1995).

[30] D. C. Radford, Nucl. Instrum. Methods Phys. Res. A **361**, 297 (1995).

[31] K. S. Krane, R. M. Steffen, and R. M. Wheeler, At. Data Nucl. Data Tables **11**, 351 (1973).

[32] H.-E. Mahnke, E. Dafni, M. H. Rafailovich, G. D. Sprouse, and E. Vapirev, Phys. Rev. C **26**, 493 (1982).

[33] T. J. Ketel, R. Kamermans, E. A. Z. M. Vervaet, and H. Verheul, Hyperfine Interact. **2**, 336 (1976).

[34] J. Cederkäll, B. Cederwall, A. Johnson, D. Seweryniak, J. Nyberg, L.-O. Norlin, J. Blomqvist, C. Fahlander, R. Wyss, A. Kerek, J. Kownacki, A. Atac, E. Adamides, E. Ideguchi, R. Julin, S. Juutinen, W. Karczmarczyk, S. Mitarai, M. Piiparinen, R. Schubart, G. Sletten, S. Törmänen, and A. Virtanen, Nucl. Phys. **A581**, 189 (1995).

[35] E. S. Paul, V. P. Janzen, D. C. Radford, D. Ward, S. M. Mullins, D. B. Fossan, D. R. LaFosse, H. Schnare, H. Timmers, P.

Vaska, R. M. Clark, and R. Wadsworth, Phys. Rev. C **50**, 2297 (1994).
[36] P. Van Nes, W. H. A. Hesselink, W. H. Dickhoff, J. J. Van Ruyven, M. J. A. de Voigt, and H. Verheul, Nucl. Phys. **A379**, 35 (1982).
[37] R. Duffait, J. van Maldeghem, A. Charvet, J. Sau, K. Heyde, A. Emsallem, M. Meyer, R. Béraud, J. Tréherne, and J. Genevey, Z. Phys. A **307**, 259 (1982).
[38] M. Fayez-Hassan, Zs. Dombrádi, Z. Gácsi, J. Gulyás, S. Brant, V. Paar, W. B. Walters, and R. A. Meyer, Nucl. Phys. **A624**, 401 (1997).
[39] S. Vajda, W. F. Piel, Jr., M. A. Quader, W. A. Watson III, F. C. Yang, and D. B. Fossan, Phys. Rev. C **27**, 2995 (1983).
[40] D. A. Viggars, H. W. Taylor, B. Singh, and J. C. Waddington, Phys. Rev. C **36**, 1006 (1987).
[41] H. Harada, T. Murakami, K. Yoshida, J. Kasagi, T. Inamura, and T. Kubo, Phys. Lett. B **207**, 17 (1988).
[42] D. R. La Fosse, D. B. Fossan, J. R. Hughes, Y. Liang, P. Vaska, M. P. Waring, and J.-Y. Zhang, Phys. Rev. C **56**, 760 (1997).
[43] R. S. Chakrawarthy and R. G. Pillay, Phys. Rev. C **54**, 2319 (1996); D. R. Lafosse *et al.* (unpublished).
[44] F. Dönau, Nucl. Phys. **A471**, 469 (1987).
[45] T. Lonnröth, S. Vadja, O. C. Kistner, and M. H. Rafailovich, Z. Phys. A **317**, 215 (1984).
[46] P. A. Butler and W. Nazarewicz, Rev. Mod. Phys. **68**, 349 (1996).
[47] G. J. Lane *et al.* (unpublished).
[48] V. P. Janzen, H. R. Andrews, B. Haas, D. C. Radford, D. Ward, A. Omar, D. Prévost, M. Sawicki, P. Unrau, J. C. Waddington, T. E. Drake, A. Galindo-Uribarri, and R. Wyss, Phys. Rev. Lett. **70**, 1065 (1993); D. R. LaFosse *et al.* (unpublished).
[49] J. M. Sears, D. B. Fossan, I. Thorslund, P. Vaska, E. S. Paul, K. Hauschild, I. M. Hibbert, R. Wadsworth, S. M. Mullins, A. V. Afanasjev, and I. Raguarsson, Phys. Rev. C **55**, 2290 (1997).
[50] A. V. Afanasjev and I. Ragnarsson, Nucl. Phys. **A628**, 580 (1998).
[51] J.-Y. Zhang, N. Xu, D. B. Fossan, Y. Liang, R. Ma, and E. S. Paul, Phys. Rev. C **39**, 714 (1989).
[52] D. B. Fossan, in *Proceedings of the Workshop on Gamma-sphere Physics* [20], p. 186.
[53] I. Ragnarsson, Phys. Lett. B **264**, 5 (1991).
[54] G. J. Lane, D. B. Fossan, I. Thorslund, P. Vaska, R. G. Allatt, E. S. Paul, L. Käubler, H. Schnare, I. M. Hibbert, N. O'Brien, R. Wadsworth, W. Andrejtscheff, J. de Graaf, J. Simpson, I. Y. Lee, A. O. Macchiavelli, D. J. Blumenthal, C. N. Davids, C. J. Lister, D. Seweryniak, A. V. Afanasjev, and I. Ragnarsson, in ''Proceedings of the Conference on Nuclear Structure at the Limits,'' Argonne, 1996, Report No. ANL/PHY-97/1 (unpublished), p. 178.
[55] I. Ragnarsson, Nucl. Phys. **A557**, 167c (1993).
[56] A. V. Afanasjev, G. A. Lalazissis, and P. Ring, in *Proceedings of the International Symposium on Exotic Nuclear Shapes*, Debrecen, Hungary, 1997, Heavy Ion Physics (in press) (also available on http://xxx.lanl.gov/abs/nucl-th/9710025); (unpublished) (available on http://xxx.lanl.gov/abs/nucl-th/9801038).